Hypervelocity Richtmyer–Meshkov instability

Ravi Samtaney[a] and Daniel I. Meiron
217-50, Applied Mathematics, Caltech, Pasadena, California 91125

(Received 17 January 1996; accepted 20 February 1997)

The Richtmyer–Meshkov instability is numerically investigated for strong shocks, i.e., for hypervelocity cases. To model the interaction of the flow with non-equilibrium chemical effects typical of high-enthalpy flows, the Lighthill–Freeman ideal dissociating gas model is employed. Richtmyer's linear theory and the impulse model are extended to include equilibrium dissociation chemistry. Numerical simulations of the compressible Euler equations indicate no period of linear growth even for amplitude to wavelength ratios as small as one percent. For large Atwood numbers, dissociation causes significant changes in density and temperature, but the change in growth of the perturbations is small. A Mach number scaling for strong shocks is presented which holds for frozen chemistry at high Mach numbers. A local analysis is used to determine the initial baroclinic circulation generation for interfaces corresponding to both positive and negative Atwood ratios. © *1997 American Institute of Physics.* [S1070-6631(97)02806-7]

I. INTRODUCTION

Recently, the Richtmyer–Meshkov environment has been the subject of extensive research, including laboratory experiments and numerical simulations.[1] In 1960, Richtmyer[2] performed the linear stability analysis of long wavelength perturbations ($A_0/\lambda \ll 1$, where A_0, λ are the initial perturbation amplitude and wavelength, respectively) on a vertical interface separating two gases (see Fig. 1) subject to an impulsive acceleration. Richtmyer considered positive Atwood ratio interfaces (the Atwood ratio is defined as $At=(\eta-1)/(\eta+1)$ where $\eta \equiv \rho_3/\rho_0$ is the density ratio of the gases across the interface) and derived linear partial differential equations. The large time asymptotic solution of these equations implied that the perturbation amplitude grows linearly with time. The prediction of linear growth was verified experimentally by Meshkov[3] in 1969 and RM (Richtmyer–Meshkov) instability became a research subject in its own right. Note that Meshkov's experimental growth rate did not quantitatively agree with Richtmyer's analysis. Grove *et al.*[4] and later Holmes *et al.*[5] noted the importance of non-linearity and compressibility effects which cause significant deviation of the growth rate from that predicted by linear theory.

Hitherto, most investigations of the Richtmyer–Meshkov instability have been confined to shocks with Mach number, $M \leqslant 4$ where M is the ratio of the shock speed to the sound speed in the gas ahead of the shock. In this paper, we present results of *hypervelocity* RM instability. The term ''hypervelocity'' is used in distinction with the term ''hypersonic.'' Hypervelocity implies not only high Mach number but also large velocities and therefore high total enthalpy. Thus, in hypervelocity RM instability, the shocks are of strength sufficient to activate dissociation/recombination chemistry and related gas-chemistry interactions. The motivation to study strong shock Richtmyer–Meshkov instability comes from its relevance to inertial confinement fusion (ICF) and astrophysical phenomena.[6,7] Experiments have been conducted with the Nova Laser[8] to understand the complicated physics in ICF. While our numerical experiments are different from the actual experiments conducted with the Nova Laser, an insight into the hydrodynamical processes at high Mach numbers is crucial to understand the more involved physics in ICF. Furthermore, the numerical investigations in this paper may be considered precursors for experiments in the free piston shock tunnel, T5, at Caltech.[9]

The primary focus of this paper is on numerical experiments of hypervelocity shock interactions with single mode (sinusoidal) interfaces. We are interested in the effect of dissociation chemistry on the growth of the perturbations and the circulation on the interface. In Sec. II, the physical parameters, governing equations and a brief description of the chemistry model are given. In Sec. III, we present a local analysis to determine the self-similar solution for oblique interfaces. This analysis enables us to quantify the baroclinic circulation generation on a sinusoidal interface. In Sec. IV we extend Richtmyer's linear theory and the impulse model to include equilibrium dissociation chemistry. In Sec. V a brief discussion of the numerical method is given, followed by detailed results of simulations in Secs. VI and VII. In addition, we examine scalings in Mach number relevant to the circulation, perturbation amplitude and growth rate for strong shocks.

II. PHYSICAL PARAMETERS, EQUATIONS AND CHEMISTRY MODEL, AND NON-DIMENSIONALIZATION

A. Physical parameters

The physical domain is a rectangular shock tube; $x(y)$ is the downstream (transverse) direction. The extent of the physical domain is $[x_l, x_r]\times[0,\lambda/2]$. The principal parameters are:

(1) The gases on either side of the interface. Typical of hypervelocity flows are high temperature effects, most notably finite rate chemical reactions of the gases present. In our investigation we use diatomic gases to elucidate the differences due to chemical reactions by only allowing for the dissociation/recombination reactions

[a]Also affiliated with the Graduate Aeronautical Laboratories, Caltech.

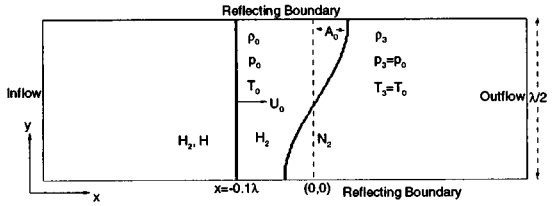

FIG. 1. Schematic of a shock interaction with single harmonic perturbed density interface. Boundary conditions are inflow/outflow in the x-direction and reflecting in the y-direction.

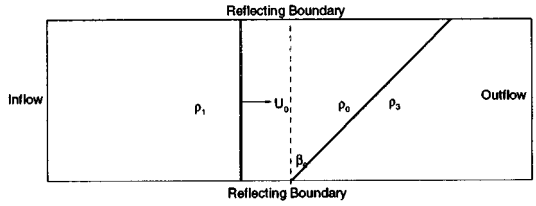

FIG. 2. Schematic of a shock interaction with a sawtooth interface inclined at β_0 to the plane of the shock.

$$A_2+S\leftrightarrow 2A+S \tag{1}$$

(with S as the third body of the interaction). The gas combinations considered here are: hydrogen-nitrogen (H_2–N_2), nitrogen-hydrogen (N_2–H_2), nitrogen-oxygen (N_2–O_2) and oxygen-nitrogen (O_2–N_2). Note that for the H_2–N_2 (N_2–H_2) and N_2–O_2 (O_2–N_2) interfaces the shock moves from a medium of lower (higher) acoustic impedance to one with a higher (lower) acoustic impedance (where the acoustic impedance is defined as the product of the density and the sound speed for the unshocked gas).

(2) The speed of the incident shock, U_0. We will refer to the gas in which the shock is initialized as the ''incident'' gas and the gas on the other side of the interface as the ''transmitted'' gas. Furthermore, although the Mach number is an ill-defined quantity for hypervelocity flow, in our investigation we define a Mach number of the shock by $M\equiv U_0/c_0$ where c_0 is the frozen speed of sound in the unshocked incident gas. Thermodynamically, one defines the square of the sound speed as the partial derivative of pressure with respect to density while holding entropy constant, i.e., $c^2=(\partial p/\partial\rho)_s$. However, in flows with chemical reactions, this derivative is not unique. Consider, for instance, the flow of a gas with non-equilibrium dissociation reaction of the form written above. Then the thermodynamic state is defined by three variables, namely the pressure p, the density ρ and q which gives the chemical state of the gas. For dissociation q may be taken as the mass fraction of the dissociated gas. Let the equilibrium dissociated composition be given by $q^*\equiv q^*(p,\rho)$. If the sound speed is calculated holding $q=q^*$ then this is termed the equilibrium speed of sound. For all other values of q the sound speed is termed the frozen speed of sound. We refer the reader to chapter VIII in the book by Vincenti and Kruger[10] for further details.

(3) The thermodynamic state of the unshocked gases, which is chosen to approximately match the conditions in the shock tunnel T5. The initial unshocked gases were maintained in thermal and mechanical equilibrium with the pressure and temperature in both gases initialized to $p_0=p_3=0.1$ atm and $T_0=T_3=298$ K, respectively. At this thermodynamic state the gases are present only in their diatomic state; consequently the frozen and equilibrium sound speeds are identical.

(4) In addition to the above parameters, the geometry of the interface has to be specified. In this paper, we examine a sinusoidal interface (i.e., interfaces perturbed by a single harmonic with initial amplitude $A(0)\equiv A_0$) as in Fig. 1 and oblique or sawtooth perturbed interfaces as shown in Fig. 2. The ratio of initial amplitude to wavelength, A_0/λ is useful in parametrizing the sinusoidal interfaces while the angle β_0 between the shock and the interface is a useful parameter for the oblique interface. We emphasize that the focus of this paper is on the evolution of the single mode interfaces and that the oblique interfaces are useful in determining the baroclinic circulation on shocked interfaces.

For the sinusoidal interface, we choose $\lambda=10$ cm in this study to approximately match the test section width of T5, the free piston shock tunnel at Caltech. A quantity of interest is the evolution of the so-called ''mixing width'' which we take to be the perturbation amplitude, $A\equiv A(t)$.

B. Equations and chemistry model

Consistent with several previous studies of the Richtmyer–Meshkov instability, the governing equations of motion are the compressible Euler equations in two dimensions written below in conservation form,

$$\mathbf{U}_t+\mathbf{F}_x(\mathbf{U})+\mathbf{G}_y(\mathbf{U})=\mathbf{S}(\mathbf{U}), \tag{2}$$

where

$$\begin{aligned}
&\mathbf{U}=\{\rho,\rho u,\rho v,E,\rho_k,\rho_k\alpha_k\}^T,\\
&\mathbf{F}(\mathbf{U})=\{\rho u,\rho u^2+p,\rho uv,(E+p)u,\rho_k u,\rho_k\alpha_k u\}^T,\\
&\mathbf{G}(\mathbf{U})=\{\rho v,\rho uv,\rho v^2+p,(E+p)v,\rho_k v,\rho_k\alpha_k v\}^T,\\
&\mathbf{S}(\mathbf{U})=\{0,0,0,0,0,\dot{w}_k\}^T.
\end{aligned} \tag{3}$$

We accept the use of the multi-dimensional compressible Euler equations as a model for real fluid behavior in spite of the reported lack of convergence in the neighborhood of vortex sheets.[11] In the above equations, ρ_k is the density of the kth gas ($k=1,2$, as only two gases are present) comprising both the diatomic and the monatomic constituents, and ρ is the total density. We choose ρ_1 (ρ_2) to be the density of the transmitted (incident) gas. Note that the subscripts ''1'' and ''2'' used here are not to be confused with those used in Sec. III and in Figs. 1 and 2 where subscripts ''0'' and ''3'' are used to indicate the unshocked incident and transmitted gases, respectively. The mass fraction of the monatomic constituent of the kth gas is α_k.

TABLE I. IDG properties.

Gas	$\rho_d(kg/m^3)$	$\theta_d(K)$	C (SI units)	κ	Temperature range (K)
Hydrogen	1800	51900	6.0E15	−1	2000–12000
Nitrogen	130000	113200	1.0E23	−3	1000–7000
Oxygen	15000	59380			1000–7000

At this point, we need to model the production terms $\dot{w}_k$. It is assumed that the chemical reactions are adequately modeled by the Lighthill Ideal Dissociating Gas model[12] used in conjunction with Freeman's chemical-reaction rate equation.[13] The law of mass action for the IDG model, which specifies the equilibrium chemical composition, may be written as

$$\frac{\alpha_k^2}{1-\alpha_k}=\frac{\rho_{d,k}}{\rho_k}\exp\left(\frac{-\theta_{d,k}}{T}\right). \tag{4}$$

In the above equation, $\theta_{d,k}$ is the dissociation temperature of the kth gas. The characteristic density $\rho_{d,k}$ is an approximation to a collection of terms in the partition function which is a weak function of temperature and is taken to be a constant by Lighthill for a wide range of temperatures. The assumption that the characteristic density is constant is equivalent to representing the sum of the equilibrium electronic excitation energies of the monatomic constituent and the vibrational excitation energies of the diatomic constituent by a single degree of freedom for the diatomic constituent which is excited at all temperatures. Thus, in the IDG model, the gas is in a state of vibrational excitation even at low temperatures. This implies a specific heat ratio $\gamma=4/3$ when no dissociation occurs at low temperatures. This is the most severe limitation of the IDG model.

The production term $\dot{w}_k$ may be written as

$$\frac{\dot{w}_k}{\rho_k}\equiv\frac{d\alpha_k}{dt}=C_k(T)\rho_k\left[(1-\alpha_k)\exp\left(\frac{-\theta_{d,k}}{T}\right)-\frac{\rho_k}{\rho_{d,k}}\alpha_k^2\right]. \tag{5}$$

The function $C_k(T)$, related to third body efficiencies in the dissociation reaction, is given by

$$C_k(T)=C_kT^{\kappa_k}. \tag{6}$$

The constants C_k, κ_k are obtained from experimental data. For the gases considered, the IDG properties and the range of temperature in which the IDG model is valid are given in Table I.

For the kth gas (composed of a diatomic and a monatomic constituent) the internal energy, enthalpy and ratio of specific heats are given by[10]

$$\begin{aligned} e_k&=(3T+\alpha_k\theta_{d,k})R_k,\\ h_k&=[(4+\alpha_k)T+\alpha_k\theta_{d,k}]R_k,\\ \gamma_k&=\frac{4+\alpha_k}{3}, \end{aligned} \tag{7}$$

where R_k is the gas constant of the diatomic constituent of the kth gas.

Ideally, in the absence of physical viscosity, the two gases cannot mix. However, in numerical simulations, the gases may mix in the vicinity of the interface due to numerical diffusion. The internal energy, enthalpy and specific heat ratio of the mixture of the two gases are given by

$$\begin{aligned} e&=\sum_k\frac{\rho_k}{\rho}e_k,\\ h&=\sum_k\frac{\rho_k}{\rho}h_k,\\ \gamma&=\frac{\Sigma_k\gamma_k\rho_kR_k}{\Sigma_k\rho_kR_k}. \end{aligned} \tag{8}$$

The total energy E is given by

$$E=\rho e+\tfrac{1}{2}\rho(u^2+v^2), \tag{9}$$

and the pressure is related to the total energy by

$$p=(\gamma-1)\left[E-\frac{1}{2}\rho(u^2+v^2)-\sum_k\rho_k\alpha_k\theta_{d,k}R_k\right]. \tag{10}$$

We emphasize that each gas in the mixture dissociates independently and does not react with the other gas. This is not a serious limitation for a mixture of hydrogen and nitrogen. For a mixture of nitrogen and oxygen, the formation of nitrogen oxides is usually small compared with the other species and may be ignored as a first approximation.

C. Non-dimensionalization

For the results presented the density, velocity, time, and length are normalized by ρ_0, c_0, λ/c_0 and λ, respectively. Note that λ/c_0 is the time taken for an acoustic wave to travel one wavelength.

The Damköhler number (a non-dimensional parameter) is defined as

$$\Omega=\frac{d\alpha}{dt}\frac{\lambda}{c_0}, \tag{11}$$

where the reaction rate is evaluated at the incident shock front. Ω may be considered as the non-dimensional reaction rate. There are three cases which must be considered:

(1) The frozen limit in which the reaction rates are zero (i.e., $\Omega=0$).
(2) The equilibrium limit in which the reaction proceeds infinitely fast. In this case $\Omega\to\infty$ and the law of mass action must be used to determine the equilibrium chemical composition.
(3) The case $0<\Omega<\infty$ for which the reaction proceeds at a finite rate. Usually this case is the one which occurs in most physical situations. However, under ''usual'' conditions the frozen and the equilibrium limits provide useful bounds. A finite Damköhler number implies an additional length scale which must be resolved in the computations. In our investigation, in all but one case, we compute the frozen and equilibrium limits. The justification for this will become apparent later on in the paper.

III. LOCAL ANALYSIS

The first physical process which occurs as the incident shock traverses the interface is refraction which means that

the incident shock wave bifurcates at the interface to form a transmitted and a reflected wave. From the point of view of the local analysis, it is important to determine the nature of the reflected wave, i.e., whether it is a rarefaction or a shock. The type of the reflected wave depends upon the strength of the shock, the densities of the gases across the interface as well as the ratio of specific heats for the gases. Yang *et al.*[14] have also derived relations to determine the nature of the reflected wave. For the purposes of this paper, based on the gas parameters used, it is sufficient to note that if the incident gas has a smaller (larger) acoustic impedance than the transmitted gas, then the reflected wave is a shock (rarefaction). This may be restated as follows. For cases of positive (negative) Atwood ratios the reflected wave is a shock (rarefaction), respectively. Henderson and Abd-El-Fattah (see Refs. 15 and 16) have classified the refraction process as ''slow-fast'' or ''fast-slow'' depending upon whether the transmitted shock speed is less or more than the incident shock speed. In terms of the terminology employed by Henderson and co-workers, for the cases considered in this paper, the interaction is slow-fast (fast-slow) if the transmitted gas has a lower (higher) density than the incident gas. Thus for slow-fast (fast-slow) interaction the reflected wave is a rarefaction (shock). In all the cases considered in this paper, the transmitted wave is a shock.

We examine the vorticity equation for an inviscid compressible flow in two dimensions:

$$\frac{D\omega/\rho}{Dt}=\frac{\nabla\rho\times\nabla p}{\rho^3}. \tag{12}$$

The term on the right in Eq. (12) is the baroclinic source term. During the refraction process a misalignment of pressure and density gradients leads to rapid vorticity deposition on the interface. We refer to this as the ''primary baroclinic circulation generation.'' Note that for the above process, we consider the pressure gradient across the shock and the density gradient across the interface. In this section we present a local analysis which is used to evaluate the primary baroclinic circulation generation. In this case, the interface is a sawtooth wave inclined at an angle β_0 to the plane of the incident shock (Fig. 2). In addition, the local analysis is a useful code validation tool.

The results for the frozen cases were obtained using the analysis of Samtaney and Zabusky.[17,18] We present here an extension of their results and perform a local analysis for the equilibrium cases ($\Omega=\infty$). Note that the subscripts ''1'' and ''2'' used in this section are not to be confused with those used in Sec. II.

A. Reflected shock case

If the acoustic impedance of the incident gas is smaller than that of the transmitted gas then the reflected wave is a shock. For sufficiently small β_0 (i.e., regular refraction) all the waves meet in a single node (see Fig. 3). Furthermore, in a small neighborhood of the node all the waves are straight lines. In this case, the Euler equations admit a self-similar or quasi-steady solution. In a frame of reference attached to the node, one may solve the jump conditions across the three shocks along with certain compatibility conditions to obtain a local solution valid in a neighborhood of the node.

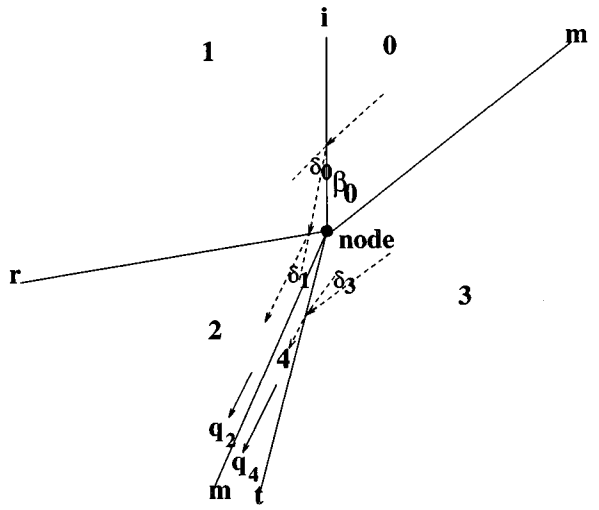

FIG. 3. Schematic of regular refraction of a shock at a low-high acoustic impedance interface. The reflected wave is a shock.

The refraction process is schematically depicted in Fig. 3. The incident, reflected, and transmitted shocks are indicated by ''i,'' ''r,'' and ''t'' respectively. The material interface or the contact discontinuity is indicated by ''m-m.'' The subscripts $i=0,1,3(k=1',2,4)$ denote the states ahead (behind) ''i'', ''r'' and ''t.'' u,v,q are the normal, tangential and total velocities, h is the enthalpy, and α is the degree of dissociation. The states ahead of the incident shock, i.e., $(\rho,u,v,q,p,T,h,\alpha)_0$ are known from the given initial data. The thermodynamic states (ρ,p,T,h,α) and total velocity q are identical behind the incident shock and ahead of the reflected shock. Let $\delta_i, i=0,1,3$ be the streamline deflections due to ''i'', ''r'' and ''t.'' There are 31 unknowns, namely: $(\rho,u,v,q,p,T,h,\alpha)_k$, $k=1',2,4$, $(\delta_i, i=0,1,3)$, (u_1,v_1), and (u_3,v_3). To solve for these unknowns we apply the jump conditions across the three shocks, i.e.,

$$\begin{aligned}&\rho_i u_i=\rho_k u_k,\\ &p_i+\rho_i u_i^2=p_k+\rho_k u_k^2,\\ &h_i+\tfrac{1}{2}q_i^2=h_k+\tfrac{1}{2}q_k^2.\end{aligned} \tag{13}$$

In addition, we have the continuity of the tangential velocity across the shocks and the definition of total velocity

$$v_i=v_k, \tag{14}$$

$$\begin{aligned}&q_k^2=u_k^2+v_k^2,\\ &q_1^2=u_1^2+v_1^2,\\ &q_3^2=u_3^2+v_3^2.\end{aligned} \tag{15}$$

The streamline deflections are given by

$$\tan\delta_i=\frac{(u_i-u_k)v_i}{(v_i^2+u_i u_k)}. \tag{16}$$

The following thermodynamic relations are used: $\alpha\equiv\alpha(\rho,T)$, $p\equiv p(\rho,T)$, and $h\equiv h(\rho,T)$ which according to the IDG model are

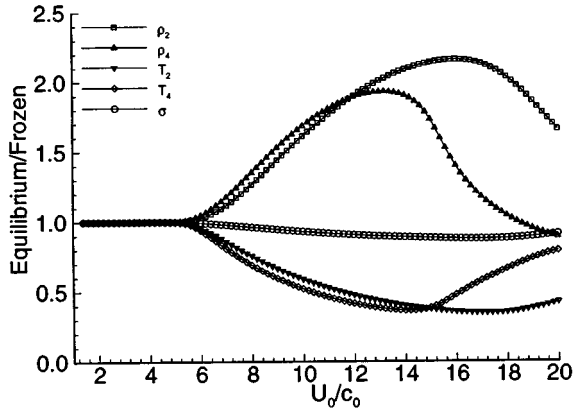

FIG. 4. Local solution for equilibrium dissociated flow normalized by the frozen solution for a $\beta_0=30°$, H_2-N_2 interface. Subscript ''2'' (''4'') represents values between the reflected (transmitted) shock and contact surface. σ is the vortex sheet strength.

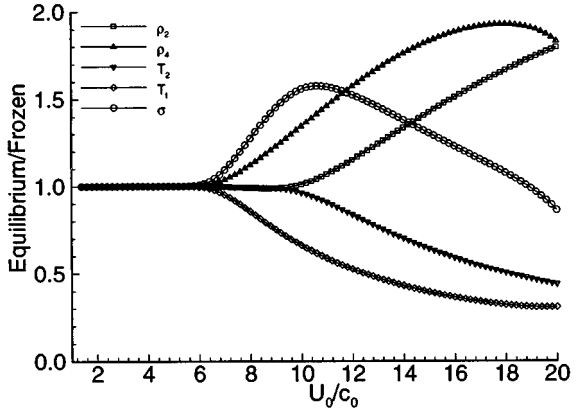

FIG. 5. Local solution for equilibrium dissociated flow normalized by the frozen solution for a $\beta_0=45°$, N_2-O_2 interface. Subscript ''2'' (''4'') represents values between the reflected (transmitted) shock and contact surface. σ is the vortex sheet strength.

$$\frac{\alpha^2}{1-\alpha}=\frac{\rho_d}{\rho}\exp\left(\frac{-\theta_d}{T}\right),$$
$$p=\rho(1+\alpha)RT, \tag{17}$$
$$h=(4+\alpha)RT+\alpha R\theta_d.$$

The compatibility conditions needed to close the above set of nonlinear algebraic equations are the continuity of pressure,

$$p_2=p_4, \tag{18}$$

and the continuity of the normal velocity component across the shocked contact discontinuity which implies

$$\delta_0=\delta_1+\delta_3. \tag{19}$$

Equations (13)–(19) are 31 algebraic equations which are solved simultaneously to obtain the local solution in the vicinity of the node. Given the incident shock strength and β_0 fixes δ_0. We then guess δ_3 and determine δ_1 using Eq. (19). A good guess can be obtained by taking the average of the minimum and maximum values of δ_3 (the maximum value for δ_3 is δ_0 and the minimum is that value of δ_3 when p_4 equals p_1). Given δ_1 and δ_3 we determine, using Newton's method, the pressure ratios p_2/p_1 and p_4/p_3 across the reflected and the transmitted shocks, respectively. We then choose a new value for δ_3 by employing the midpoint bisection method and iterate until $p_2=p_4$. Of particular interest is the magnitude of the vortex sheet strength given by

$$\sigma=|q_2-q_4|. \tag{20}$$

For a H_2-N_2 interface inclined at $\beta_0=30°$ the density and temperature behind the reflected and transmitted shocks and the vortex sheet strength for the equilibrium limit, normalized by the frozen limit, are plotted in Fig. 4. The differences due to dissociation occur at about $M=6$. While the density and the temperature behind the reflected and the transmitted shock show appreciable differences due to dissociation, the change in the vortex sheet strength is small. For $M>15$ all the diatomic species have dissociated completely and the resulting gas behaves as a monatomic perfect gas. In fact the slope of the Hugoniot becomes negative. This causes the reversal of the trends for the changes in density and temperature. We caution the reader that results for $M>15$ may not be accurate as the temperature behind the transmitted shock is significantly beyond the range of temperatures for which the IDG model is valid.

A similar analysis was performed for the N_2-O_2 interface. The results for $\beta_0=45°$ are shown in Fig. 5. For $M<18$ the vortex sheet strength for the equilibrium limit is larger than the frozen limit.

B. Reflected rarefaction case

In this section we present a local analysis for the case when the reflected wave is a rarefaction (denoted as ''e'' in Fig. 6). In this case the jump conditions across the reflected shock are replaced by the equations of a Prandtl–Meyer isentropic expansion. The streamline deflection across the expansion fan is given by

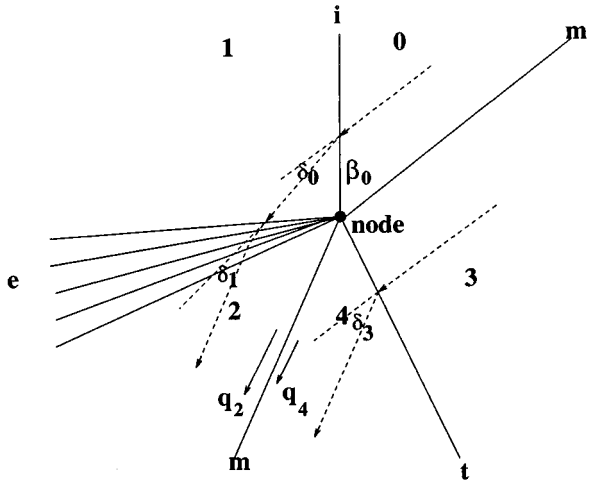

FIG. 6. Schematic of regular refraction of a shock at a high-low acoustic impedance interface. The reflected wave is a centered rarefaction.

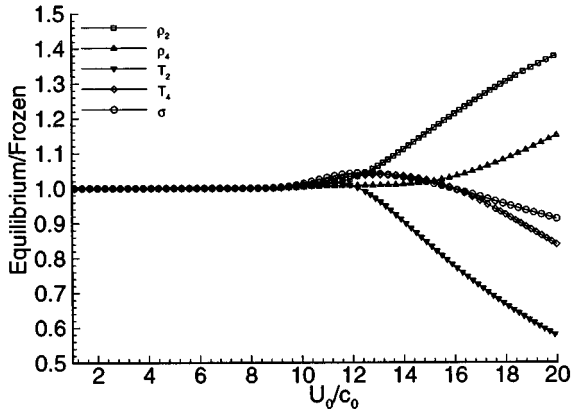

FIG. 7. Local solution for equilibrium dissociated flow normalized by the frozen solution for a $\beta_0=15°$, N_2-H_2 interface. Subscript ''2'' (''4'') represent values between the reflected (transmitted) waves and contact surface. σ is the vortex sheet strength.

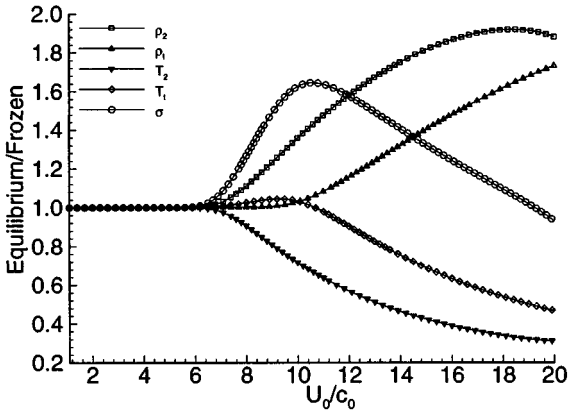

FIG. 8. Local solution for equilibrium dissociated flow normalized by the frozen solution for a $\beta_0=45°$, O_2-N_2 interface. Subscript ''2''(''4'') represent values between the reflected (transmitted) waves and contact surface. σ is the vortex sheet strength.

$$\delta_1=\int_1^2\left(\frac{q^2}{c^2}-1\right)^{1/2}\frac{dq}{q}, \tag{21}$$

where c is the *equilibrium* sound speed given for a gas modeled as an IDG by

$$\frac{c}{RT}=\frac{\alpha(1-\alpha^2)\left(1+2T/\theta_d\right)+(8+3\alpha-\alpha^3)\left(T/\theta_d\right)^2}{\alpha(1-\alpha)+3(2-\alpha)\left(T/\theta_d\right)^2}. \tag{22}$$

In solving Eq. (21), the entropy (given below for a gas modeled as an IDG) is held constant:

$$\frac{s}{R}=3\log\frac{T}{\theta_d}+\alpha(1-2\log\alpha)$$
$$-(1-\alpha)\log(1-\alpha)-(1+\alpha)\log\frac{\rho}{\rho_d}. \tag{23}$$

The continuity of normal velocity across the shocked contact discontinuity implies that

$$\delta_0+\delta_1=\delta_3. \tag{24}$$

As for the reflected shock case, we obtain the local solution in the vicinity of the node where all the three waves meet provided the angle β_0 is small enough to admit regular refraction. For a N_2-H_2 interface inclined at $\beta_0=15°$ the density and temperature behind the reflected centered expansion wave and transmitted shock, and the vortex sheet strength for the equilibrium case normalized by the frozen case are shown in Fig. 7. Effects of dissociation are apparent for $M\geqslant 10$. The vortex sheet is stronger for the equilibrium chemistry case for $5.9\leqslant M\leqslant 15.8$ and weaker for $M>15.8$. This effect could be due to the recombination of nitrogen across the expansion wave.

A similar analysis was performed for the O_2-N_2 interface. The results for $\beta_0=45°$ are shown in Fig. 8. The vortex sheet strength increases whenever chemistry is active for $M<18$.

C. Primary baroclinic circulation for a sinusoidal interface

The above analysis enables us to determine the primary baroclinic circulation generation on a sinusoidal interface by integrating the vortex sheet strength over the *original* length s of the interface (and neglecting curvature effects) as

$$\Gamma_1=\int \sigma(s)\frac{\cos\beta_0(s)}{\cos(\beta_0(s)-\delta_3(s))}ds. \tag{25}$$

In Eq. (25) the integrand exists if the refraction remains regular during the time the incident shock traverses the interface. The maximum angle between the interface and the shock is given by $\arctan(A_0k)$ which for $A_0/\lambda=0.1$ is 32.14°. For the interaction of a $M=10$ shock with a H_2-N_2 interface, the integration is possible because the refraction is regular when the incident shock traverses the interface. If the refraction becomes irregular when the shock traverses the interface, then the local analysis cannot be used to determine the primary circulation generation. For such cases, we may use the following asymptotic result[17,18]

$$\Gamma_1=2A_0\left(\frac{\partial\sigma}{\partial\beta_0}\right)_{\beta_0=0}, \tag{26}$$

where the derivative in the above equation is evaluated numerically in the equilibrium chemistry case. The total circulation at the end of the refraction process was quantified for sinusoidal interfaces with $A_0/\lambda=0.1$ in numerical simulations (see Secs. VI and VII). The comparison between the theoretical circulation Γ_1 and numerical baroclinic circulation Γ is summarized in Table II. We determined the circulation for the N_2-H_2 interface employing the asymptotic result given by Eq. (26).

IV. THE LINEAR THEORY AND IMPULSE MODEL FOR AN IDG

In this section we extend the linear theory and impulse model to flows with equilibrium dissociation chemistry for the case of a reflected shock wave. Richtmyer[2] derived a wave equation governing the pressure disturbances

TABLE II. Comparison of circulation from local analysis with numerical simulations. The interface is sinusoidal with $A_0 = 0.1$.

Interface	M	Chemistry	Γ_1	Γ
N_2–H_2	12	Frozen	2.246	2.157
N_2–H_2	12	Equilibrium	2.334	2.166
N_2–H_2	18	Frozen	3.241	3.161
N_2–H_2	18	Equilibrium	3.081	2.984
H_2–N_2	10	Frozen	−1.191	−1.159
H_2–N_2	10	Equilibrium	−1.103	−1.081
H_2–N_2	15	Frozen	−1.720	−1.763
H_2–N_2	15	Equilibrium	−1.525	−1.543

by linearizing the compressible Euler equations. In linear theory any quantity $q(x,y,t)$ is expressed as $q(x,y,t) = q^0(x,t) + q^1(x,t)\exp(iky)$ where the superscript ''0'' denotes the basic state while ''1'' denotes the perturbation. The basic state is calculated by solving a one dimensional shock-contact discontinuity interaction and consists of a contact discontinuity, and a reflected and a transmitted shock.

Richtmyer's equations are stated below (in our notation):

$$\frac{\partial^2 p_l^1}{\partial t^2} = c_l^2\left(\frac{\partial^2 p_l^1}{\partial x^2} - k^2 p_l^1\right), \tag{27}$$

where p_l^1 is the pressure disturbance and $l = 2,4$ depending upon whether this equation is solved in region ''2'' (region between the reflected shock and the contact discontinuity) or region ''4'' (region between the transmitted shock and the contact discontinuity). In a frame of reference moving with the mean velocity of the contact, denote the speeds of the transmitted shock and the reflected shock as W_t and W_r respectively (both are taken to be positive numbers). Furthermore denote the post-shock contact amplitude and the amplitudes of the perturbed transmitted and reflected shock fronts as A_0, A_t, A_r respectively. The boundary conditions at the transmitted shock are

$$\dot{A}_t(t) = C_{ts1} p_4^1(W_t t, t), \tag{28}$$

$$\frac{p_4^1(w_t t, t)}{dt} = C_{ts2}\left.\frac{\partial p_4^1(x,t)}{\partial x}\right|_{x = W_t t} + C_{ts3} A_t(t), \tag{29}$$

where the coefficients are defined by

$$C_{ts1} \equiv \frac{1}{2}\frac{1}{\rho_4^0 - \rho_3^0}\left[\frac{1}{W_t} - \frac{W_t}{K_t (c_4^0)^2}\right], \tag{30}$$

$$C_{ts2} \equiv [W_t^2 - (c_4^0)^2] \Bigg/ \left[W_t + \frac{(c_4^0)^2}{2W_t} + \frac{W_t}{2K_t}\right], \tag{31}$$

$$C_{ts3} \equiv k^2 (c_4^0)^2 \rho_4^0 u_3^0 W_t \Bigg/ \left[W_t + \frac{(c_4^0)^2}{2W_t} + \frac{W_t}{2K_t}\right], \tag{32}$$

and K_t is the slope of the Hugoniot denoted as $P_h(V)$ for the transmitted shock, and is given by

$$K_t \equiv -\frac{1}{(c_4^0 \rho_4^0)^2}\left.\frac{dP_h(V)}{dV}\right|_{V = 1/\rho_4^0}. \tag{33}$$

Similarly the boundary conditions at the reflected shock are

$$\dot{A}_r(t) = -C_{rs1} p_2^1(W_r t, t), \tag{34}$$

$$\frac{p_2^1(W_r t, t)}{dt} = -C_{rs2}\left.\frac{\partial p_2^1(x,t)}{\partial x}\right|_{x = W_r t} + C_{rs3} A_r(t), \tag{35}$$

where the coefficients are defined by

$$C_{rs1} \equiv \frac{1}{2}\frac{1}{\rho_2^0 - \rho_1^0}\left[\frac{1}{W_r} - \frac{W_r}{K_r (c_2^0)^2}\right], \tag{36}$$

$$C_{rs2} \equiv [W_r^2 - (c_2^0)^2] \Bigg/ \left[W_r + \frac{(c_2^0)^2}{2W_r} + \frac{W_r}{2K_r}\right], \tag{37}$$

$$C_{rs3} \equiv k^2 (c_2^0)^2 \rho_2^0 u_1^0 W_r \Bigg/ \left[W_r + \frac{(c_2^0)^2}{2W_r} + \frac{W_r}{2K_r}\right], \tag{38}$$

and K_r is the slope of the Hugoniot, denoted as $P_l(V)$ for the reflected shock, and is given by

$$K_r \equiv -\frac{1}{(c_2^0 \rho_2^0)^2}\left.\frac{dP_l(V)}{dV}\right|_{V = 1/\rho_2^0}. \tag{39}$$

The boundary conditions at the interface are

$$p_2^1 = p_4^1, \tag{40}$$

$$\frac{d^2 A_0(t)}{dt^2} = -\frac{1}{\rho_2^0}\left.\frac{dp_2^1}{dx}\right|_{x = 0-} = -\frac{1}{\rho_4^0}\left.\frac{dp_4^1}{dx}\right|_{x = 0+}. \tag{41}$$

So far we have just repeated what was derived by Richtmyer. To include equilibrium dissociation chemistry we require the following modifications:

(1) The basic state must now be solved for flows with equilibrium chemistry. The equations developed for the local analysis may be used with $\beta_0 = 0$.
(2) The sound speed in Eq. (27) must be the *equilibrium* sound speed for an IDG defined by Eq. (22).
(3) The Hugoniots used must be for an IDG. The slope of the Hugoniots, K_t and K_r are calculated by numerical differentiation.

It is convenient to employ the transformation $\xi \equiv x/t$ as done by Yang *et al.*[14] This ensures that the boundaries are fixed. The wave equation governing the pressure perturbation now becomes (dropping the super- and subscripts)[14]

$$\frac{\partial^2 p}{\partial t^2} = \frac{c^2 - \xi^2}{t^2}\frac{\partial^2 p}{\partial \xi^2} + \frac{2\xi}{t}\frac{\partial^2 p}{\partial t \partial \xi} - \frac{2\xi}{t}\frac{\partial p}{\partial \xi} - k^2 p. \tag{42}$$

Note that the boundary conditions have to be modified according to the transformation $\xi \equiv x/t$. Since time t appears in the denominator in Eq. (42), we make the transformation $s = \log(t)$ to increase the accuracy of the solution for small times. Equation (42) is then written as the following two equations which are solved numerically by a second-order accurate finite difference method:

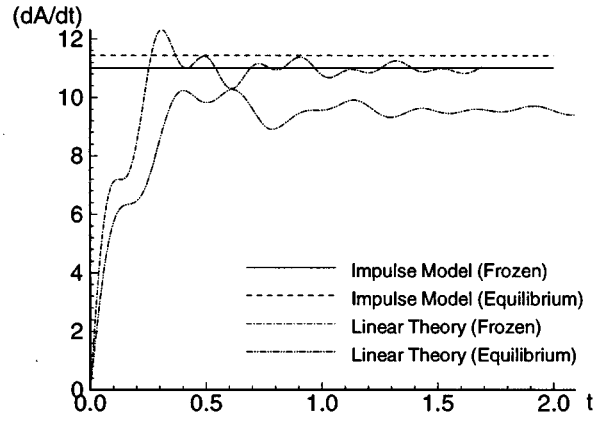

FIG. 9. Linear theory and Impulse model growth rates of the perturbation, normalized by the initial perturbation amplitude to wavelength ratio A_0/λ, for an $M=10$ shock interaction with a H_2–N_2 interface.

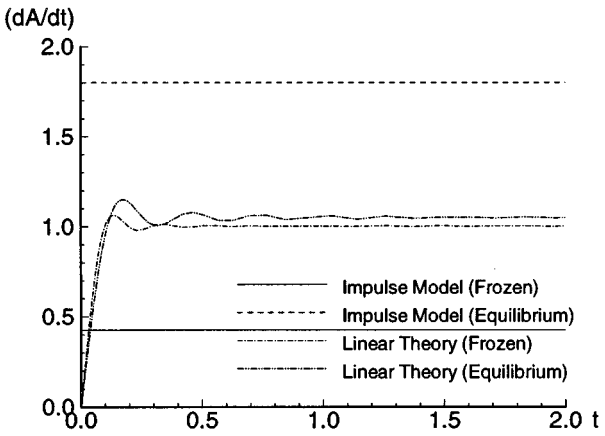

FIG. 10. Linear theory and impulse model growth rates of the perturbation, normalized by the initial perturbation amplitude to wavelength ratio A_0/λ, for an $M=12$ shock interaction with a N_2–O_2 interface.

$$\frac{\partial p}{\partial s}=q,$$

$$\frac{\partial q}{\partial s}=(c^2-\xi^2)\frac{\partial^2 p}{\partial \xi^2}+2\xi\frac{\partial^2 q}{\partial \xi}-2\xi\frac{\partial p}{\partial \xi}+q-k^2t^2p. \tag{43}$$

We developed a code to solve the equations given above [Eq. (43)]. The code is initialized by employing the small t solution given by Yang *et al.*[14]

We now modify the impulse model to include equilibrium dissociation chemistry. The impulse model proposed by Richtmyer[2] for the growth rate of perturbations is as follows:

$$\dot{A}(t)=kA_0\Delta U\frac{\eta-1}{\eta+1}. \tag{44}$$

In Eq. (44), k is the wave number, and ΔU is the change in the mean velocity of the interface. Richtmyer further suggested the use of post-shock quantities in Eq. (44). He derived the initial compression of the amplitude from kinematic considerations as

$$\frac{A_{0+}}{A_0}=1-\frac{\Delta U}{U_0}, \tag{45}$$

where U_0 is the velocity of the incident shock and $A_{0+}(A_0)$ are the post (pre) shock amplitudes of the perturbation. The domain of validity of the impulse model was explored by Yang *et al.*[14] It is clear that the impulse model suggests a linear dependence in M for $M\gg 1$ which is consistent with the high Mach number scaling discussed later in this paper. In the limit, $\beta_0\to 0$ one can reduce the equations of local analysis (see Sec. III) to get a set of algebraic equations which are solved to get the solution of a one-dimensional shock contact interaction for both the frozen and equilibrium chemistry cases. The contact speed ΔU and the post-shock amplitude A_{0+} and Atwood number are substituted in Eq. (44) to obtain the impulse model growth rate for equilibrium dissociation chemistry.

In Fig. 9 we plot the growth rates, normalized by the initial perturbation amplitude to wavelength ratio A_0/λ, for a H_2–N_2 interface for an $M=10$ incident shock. The late time growth rate from the linear theory is smaller for the equilibrium chemistry case than the frozen case by about 15%. It is interesting to note that times at which the crests and troughs appear are different for two cases. Later we shall demonstrate that even for $A_0/\lambda=0.01$ the nonlinearity manifests itself very rapidly. For frozen chemistry the impulse model growth rate agrees with the late-time asymptotic growth rate from the linear theory. On the other hand, the equilibrium impulse model indicates a slightly larger growth rate than the frozen chemistry impulse model. While the initial compression is larger (i.e., A_{0+} is smaller) for the equilibrium chemistry case, both the ΔU as well as the post-shock Atwood ratio are larger in the equilibrium chemistry case and the net result is a larger impulse model growth rate in the presence of equilibrium chemistry. Also, for flows with equilibrium chemistry the impulse model differs from the late-time asymptotic growth rate from the linear theory.

In Fig. 10 we plot the growth rates, normalized by A_0/λ, for a N_2–O_2 interface for an $M=12$ incident shock. In this low Atwood number case, the agreement between the impulse model growth rates and the linear theory is quite poor. In fact the equilibrium impulse model growth rate differs from the frozen impulse model growth rate by a factor of 4.

V. NUMERICAL METHOD

The numerical method employed to obtain the simulation results in the next section is a second order accurate Equilibrium Flux Method (EFM).[19] Note that EFM does not require the calculation of the sound speed which is desirable for finite Ω cases. EFM, however, is more diffusive than Godunov type methods. Macrossan[20] has extended EFM to second order accuracy including IDG chemistry, and discusses the diffusion in EFM in detail. We extend the method further to include a mixture of two ideally dissociating gases which occurs at the interface due to numerical diffusion. Furthermore, our approach to achieve second order accuracy is different from that of Macrossan.

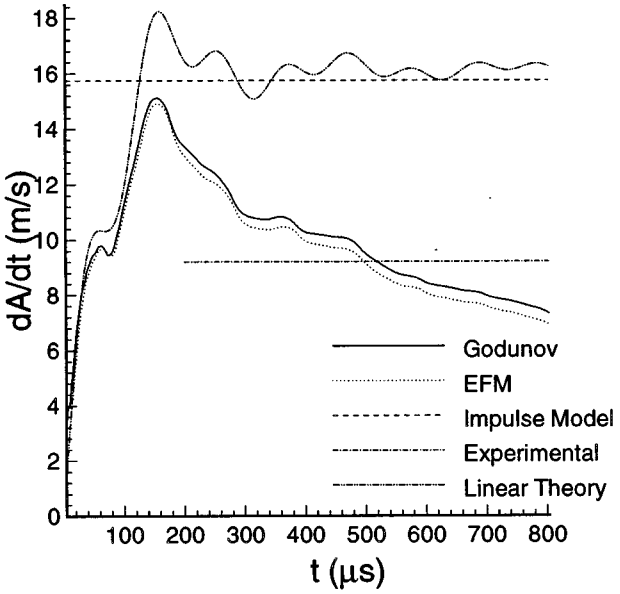

FIG. 11. Growth rate for an $M=1.2$ shock interaction with Air–SF6 interface.

In the numerical calculation, operator splitting is employed. This means that the equations [Eq. (2)] are solved in two parts. In the first or ''hydrodynamical'' part, the compressible Euler equations (with $\mathbf{S}=0$) are solved. In the second step or ''chemistry'' part, we determine the composition of the gases. We solve either Eq. (4) which is the law of mass action (for $\Omega\rightarrow\infty$) for each gas or solve Eq. (5) which governs the finite rate chemistry (finite Ω) in each computational cell. The details of the numerical method are relegated to the Appendix.

For all our simulations, the physical domain is divided into a uniform grid. We take care that internal waves do not reach the left or the right boundary during the simulations. Hence the left boundary condition is just the uniform flow behind the incident shock while the boundary condition on the right is simply the initial quiescent transmitted gas state. The boundary conditions are reflecting in the y-direction.

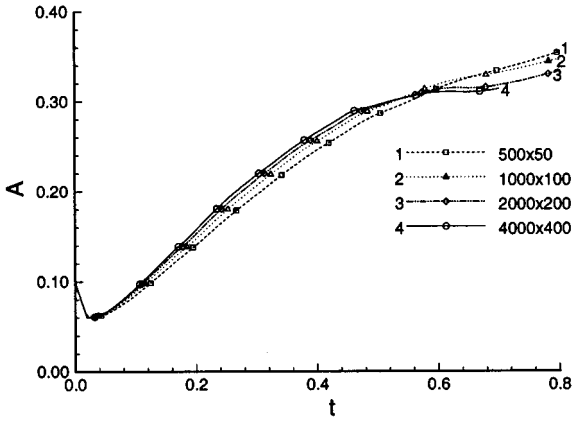

FIG. 13. Amplitude of perturbation for different grid sizes, for an $M=10$ shock interaction with a $A_0/\lambda=0.1$ H_2–N_2 interface. Frozen chemistry.

The code was implemented on the 512 node Intel Paragon which is a message-passing parallel machine, and achieved roughly 1.4 GFLOPS performance on 100 processors. Mesh archetypes[21] were used to achieve domain decomposition and communication between processors and to aid in porting the serial version of EFM to a parallel computer. The best load balancing was achieved by slicing the domain in the y-direction only.

A. Code validation

For the purposes of code validation we choose the case of a $M=1.2$ incident shock and an interface between air and sulphur-hexaflouride with $A_0=2.4$ mm, $\lambda=37.5$ mm. These were the parameters of Benjamin's experiment[22] and numerically simulated using a front-tracking method by Grove *et al.*[4] and Holmes *et al.*[5] The growth rate for this case is shown in Fig. 11. We observe that the second order EFM agrees well with the second order Godunov method (a brief

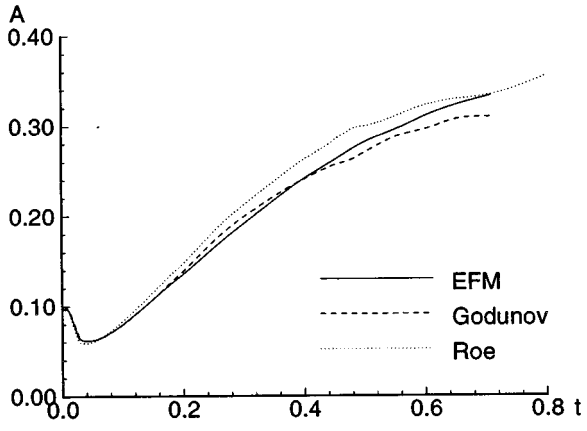

FIG. 12. Perturbation amplitude for different numerical methods for an $M=10$ shock interaction with a $A_0/\lambda=0.1$ H_2–N_2 interface. Frozen chemistry.

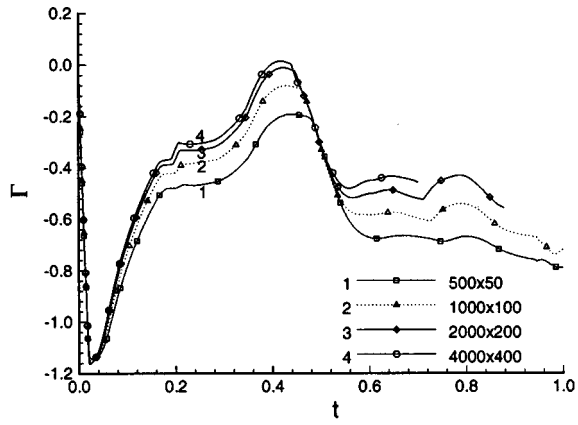

FIG. 14. Total circulation for different grid sizes, for an $M=10$ shock interaction with a $A_0/\lambda=0.1$ H_2–N_2 interface. Frozen chemistry.

description of this method is given in Reference 17) and moreover, the plots of the growth rate look remarkably similar to Fig. 2(b) in Reference 4.

B. Comparison between EFM, Godunov and Roe methods

We now compare EFM with two standard methods of computing the fluxes namely the Godunov and the Roe methods. The test case used is that of a $M=10$ shock interaction with a $A_0/\lambda=0.1$ H_2-N_2 interface with frozen chemistry on a mesh of size 500×50. We employed a second order Godunov method with slope limiting and observed severe numerical oscillations in the y-direction in a localized region behind the transmitted shock. Note that these oscillations were absent for the $M=1.2$ case described above in the section on code validation. While it is believed that the application of additional numerical viscosity will mitigate these effects we did not choose to do so. Therefore, the Godunov method was deemed unsuitable for strong shock cases. Meloon[23] provided us with results from a second order Roe method. The amplitude of perturbation for the EFM, Roe and Godunov method is plotted in Fig. 12. For times beyond $t=0.4$ the oscillations present in the Godunov case have considerably contaminated the field and quantification of the perturbation amplitude is not very accurate. Nevertheless, the maximum difference in the amplitude between the Roe method and the EFM method was less than 5%, while the maximum difference between the EFM and Godunov method was about 7%. Considering the fact that these three numerical methods are quite different this small difference is encouraging.

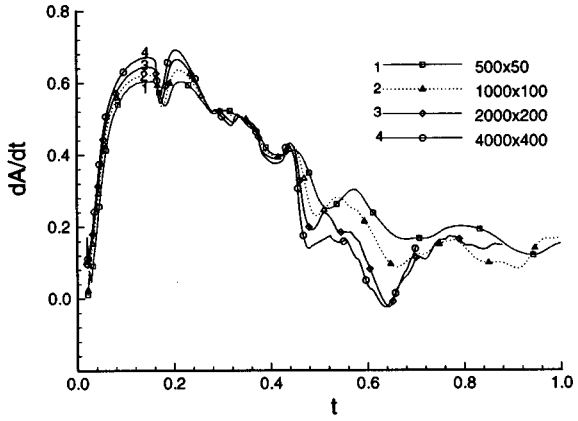

FIG. 15. Growth rate of perturbation for different grid sizes, for an $M=10$ shock interaction with a $A_0/\lambda=0.1$ H_2-N_2 interface. Frozen chemistry.

C. Convergence study

In this section we present the results of a convergence study of some gross features for a $M=10$ shock interaction with a $A_0/\lambda=0.1$ H_2-N_2 interface with frozen chemistry with grid sizes: (1) 500×50, (2) 1000×100 (3) 2000×200, and (4) 4000×400. Recently, Samtaney and Pullin[11] have

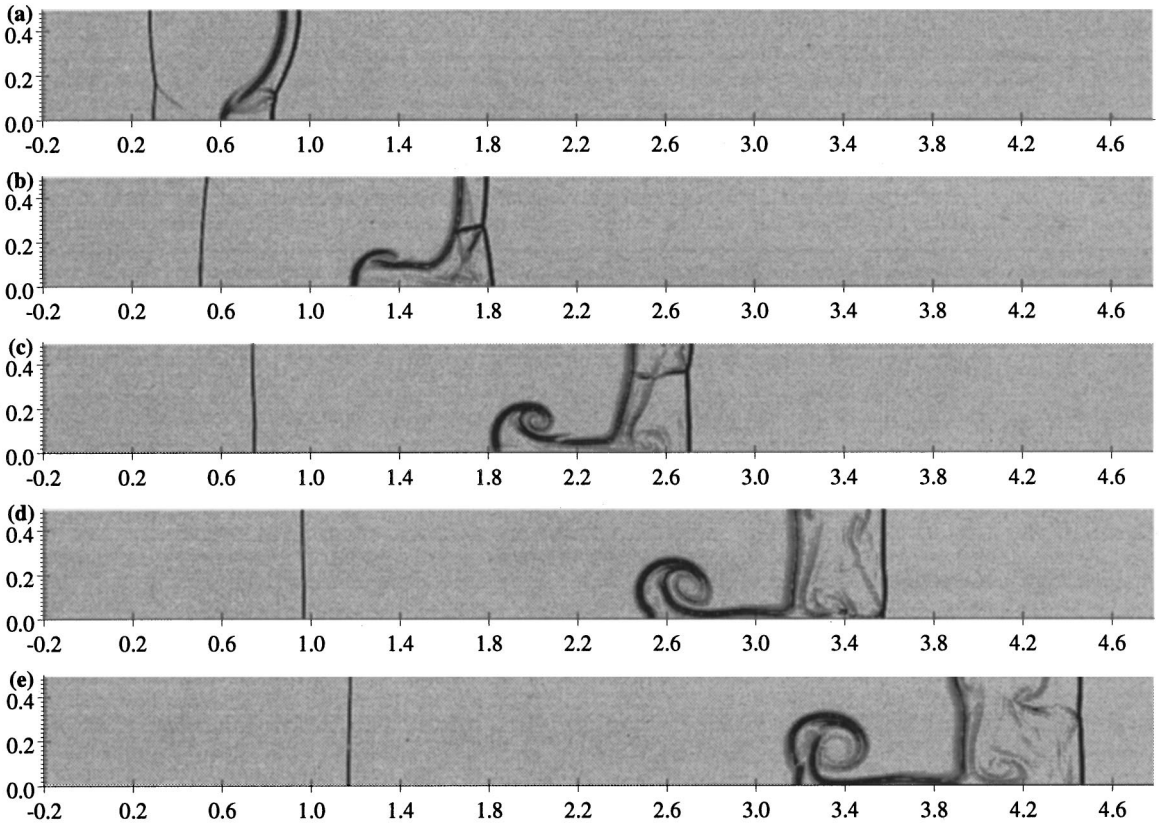

FIG. 16. Time sequence of numerical shadowgraphs for an $M=10$ shock interaction with a $A_0/\lambda=0.1$ H_2-N_2 interface. Frozen chemistry. Times shown are: (a) 0.166, (b) 0.345, (c) 0.523 (d) 0.700 and (e) 0.878.

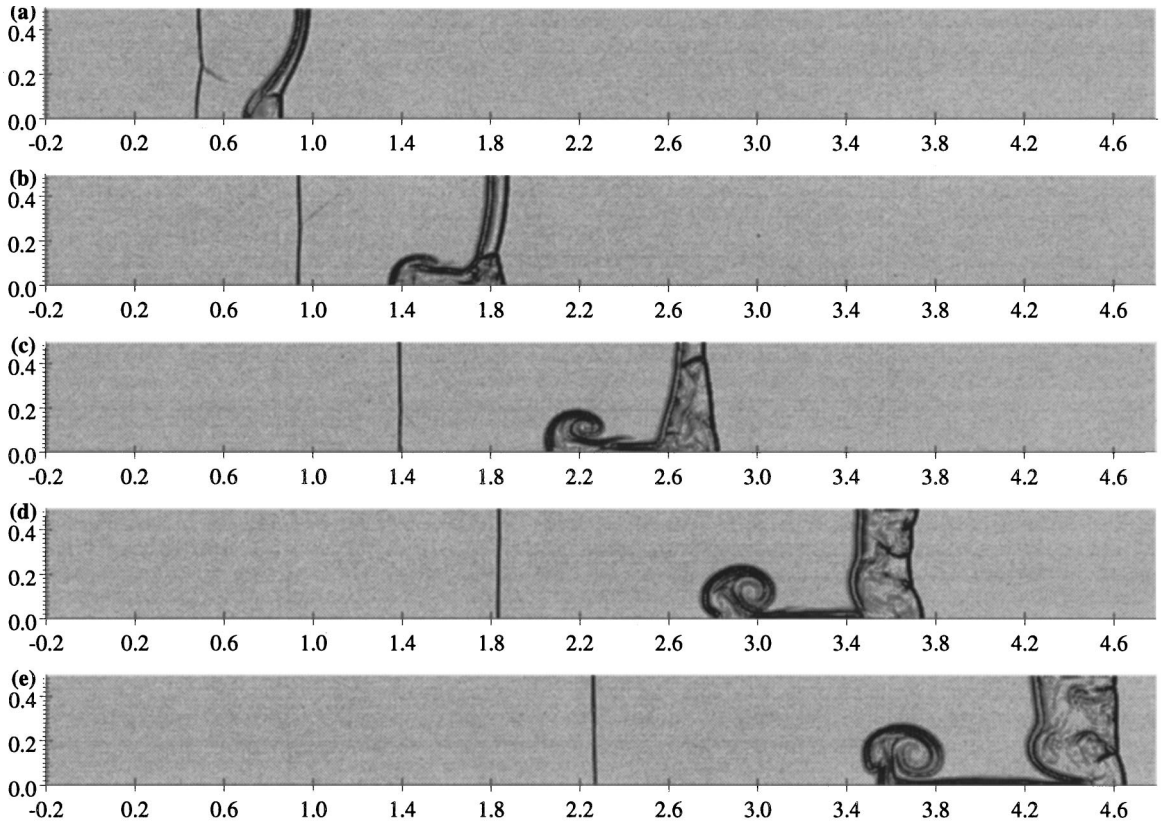

FIG. 17. Time sequence of numerical shadowgraphs for an $M=10$ shock interaction with a $A_0/\lambda=0.1$ H_2-N_2 interface. Equilibrium chemistry. Times shown are: (a) 0.167, (b) 0.346, (c) 0.524 (d) 0.703 and (e) 0.881.

speculated on convergence of computations to the weak solution of the compressible Euler equations in the presence of vortex sheets. Their computations indicate a lack of convergence with mesh refinement in the vicinity of vortex sheets. Lack of convergence was also reported by Mulder *et al.*[24] in their inviscid numerical computations of Rayleigh–Taylor and Kelvin–Helmholtz instabilities. The only convergence one may hope to achieve is for integrated quantities such as circulation and perturbation amplitude. For each resolution, the following quantities are plotted as a function of time in Figs. 13, 14 and 15: the perturbation amplitude (A), the total circulation in the domain (Γ), and the instantaneous growth rate of the perturbation amplitude (dA/dt) (taken as the instantaneous pointwise difference in the velocities at the top and bottom portion of the interface). Clearly, the computations have converged for early times. At intermediate and late times we observe that the differences between successive doubling of the grid sizes decreases. In fact the difference between grids (3) and (4) is quite small especially for $t\leqslant 0.6$. This leads us to believe that convergence will be achieved for even larger grid sizes. As will be explained in detail later, the poor convergence in circulation at late times is attributed to the presence of shear layers in the flow. Theoretically, these shear layers which arise spontaneously at triple points are vortex sheets which diffuse due to numerical viscosity. Note that triple points are points where three shocks meet and the jump conditions across all shocks are satisfied if a contact discontinuity is included in the solution.[25] The triple points arise in our case at the shock front which kinks to form a Mach stem near a solid boundary to satisfy the boundary conditions. The situation is analogous to irregular shock reflection at a solid wall where we have a three shock system and a contact discontinuity all meeting at one point namely the triple point. Although higher resolution simulations are desirable, these prove to be computationally prohibitive at the present time. Nonetheless, overall qualitative physics may still be extracted from these simulations. The simulation results presented below are performed using the 2000×200 grid; the results for the Mach scaling and the finite rate chemistry cases were obtained for the 1000×100 grid.

VI. SIMULATION RESULTS: HIGH ATWOOD RATIO INTERFACES

In this section we present detailed examinations of the flow fields for two specific cases: a Mach $M=10$ interaction with a H_2-N_2 sinusoidal interface and a Mach $M=18$ shock interaction with a N_2-H_2 sinusoidal interface. This is followed by an examination of Mach number scaling for these large Atwood ratio cases.

A. Low-high acoustic impedance case: H_2-N_2 interface

In this section we present results for a $M=10$ shock interaction with a H_2-N_2 interface perturbed sinusoidally with $A_0/\lambda=0.1$. The physical domain extent in the x-direction is $[x_l,x_r]\equiv[-0.2\lambda,4.8\lambda]$. The first interaction

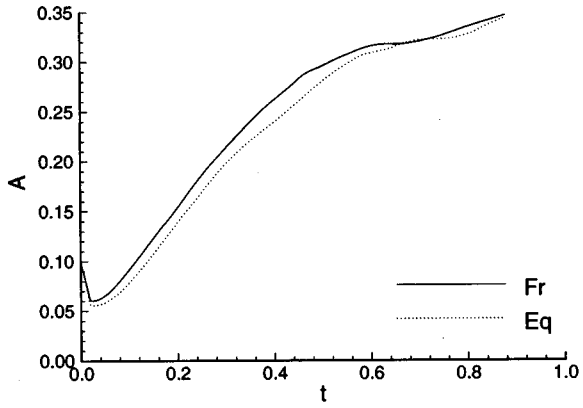

FIG. 18. Amplitude of the perturbation for an $M=10$ shock interaction with a $A_0/\lambda=0.1$ H_2-N_2 interface. Fr (Eq) implies frozen (equilibrium) chemistry.

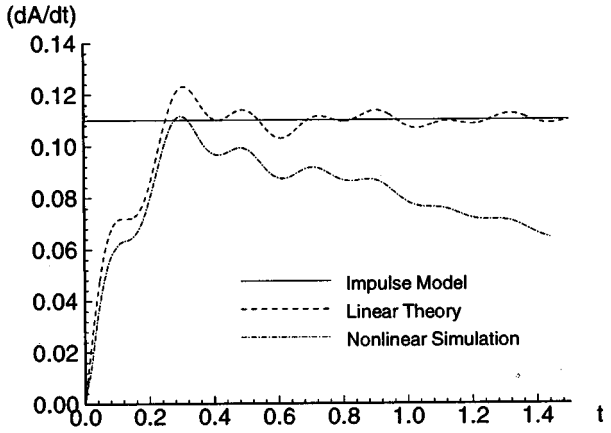

FIG. 20. Growth rate of the perturbation for an $M=10$ shock interaction with a $A_0/\lambda=0.01$ H_2-N_2 interface. Frozen chemistry.

between the shock and the interface is the very rapid shock refraction process. In this case the transmitted and the reflected waves are both shock waves. The transmitted shock moves at a slower speed relative to the incident shock while the reflected shock moves to the right in the laboratory frame of reference. In Figs. 16 and 17 numerical shadowgraph images (generated by taking the Laplacian of density) are shown at various times during the simulation for the frozen and equilibrium dissociation chemistry cases respectively. The discontinuities in the flow are clearly seen in the numerical shadowgraphs. The mean velocities in the x-direction of the primary waves (the reflected shock, the transmitted shock and the contact discontinuity) are larger for the equilibrium case than the frozen case. However, for the equilibrium chemistry case, the transmitted and the reflected shock lie closer to the interface than the frozen case. This effect is due to the larger compression of the gases for the equilibrium case than the frozen case. The contact discontinuity rolls up and gives rise to the familiar mushroom shape of the interface. Nitrogen penetrates into hydrogen as a strong spike. The hydrogen penetration into nitrogen is in the form of a bubble which assumes a vertically flat shape in a short time, and the bubble velocity approaches the velocity of the contact from a one-dimensional shock-contact interaction. Thus, the growth of the perturbation is mostly due to the relative velocity of the strong spike, and the evolution of the interface is very asymmetric unlike the near-symmetric evolution for very weak shocks.

The peak density was approximately $135\rho_0$ in the frozen chemistry case and $290\rho_0$ in the equilibrium chemistry case. The ratio of the peak density (temperature) in the equilibrium chemistry to the frozen chemistry case is approximately 2.1(0.4). This, a well-known effect, is due to endothermic dissociation. During the simulation, the peak temperature in N_2 at $t=0.166$ and $t=0.878$ was 8620 K and 8725 K, respectively for the equilibrium chemistry case. Thus in certain small localized regions we are beyond the domain of validity of the IDG model. However we believe that this is not a serious shortcoming. The maximum level of dissociation of hydrogen (nitrogen) molecules is about 20%(36%).

Aside from differences in the speed of the waves and local magnitudes of the density and temperature, the geom-

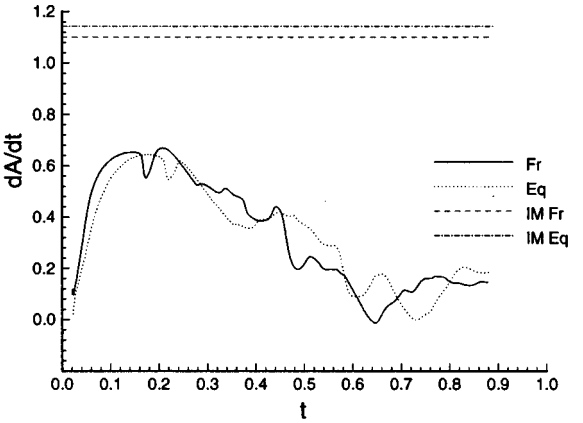

FIG. 19. Growth rate of the perturbation for an $M=10$ shock interaction with a $A_0/\lambda=0.1$ H_2-N_2 interface. The horizontal dotted lines are the impulse model (IM) growth rates.

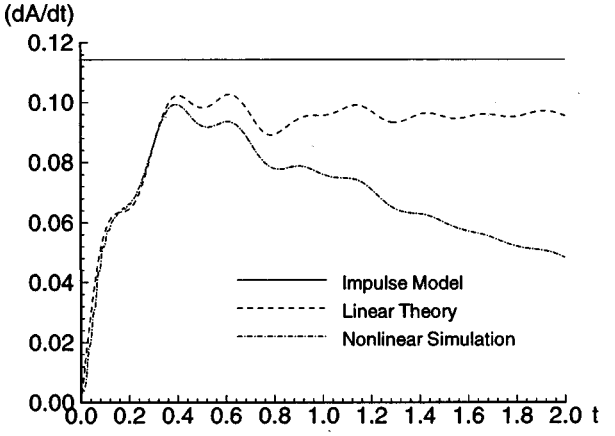

FIG. 21. Growth rate of the perturbation for an $M=10$ shock interaction with a $A_0/\lambda=0.01$ H_2-N_2 interface. Equilibrium chemistry.

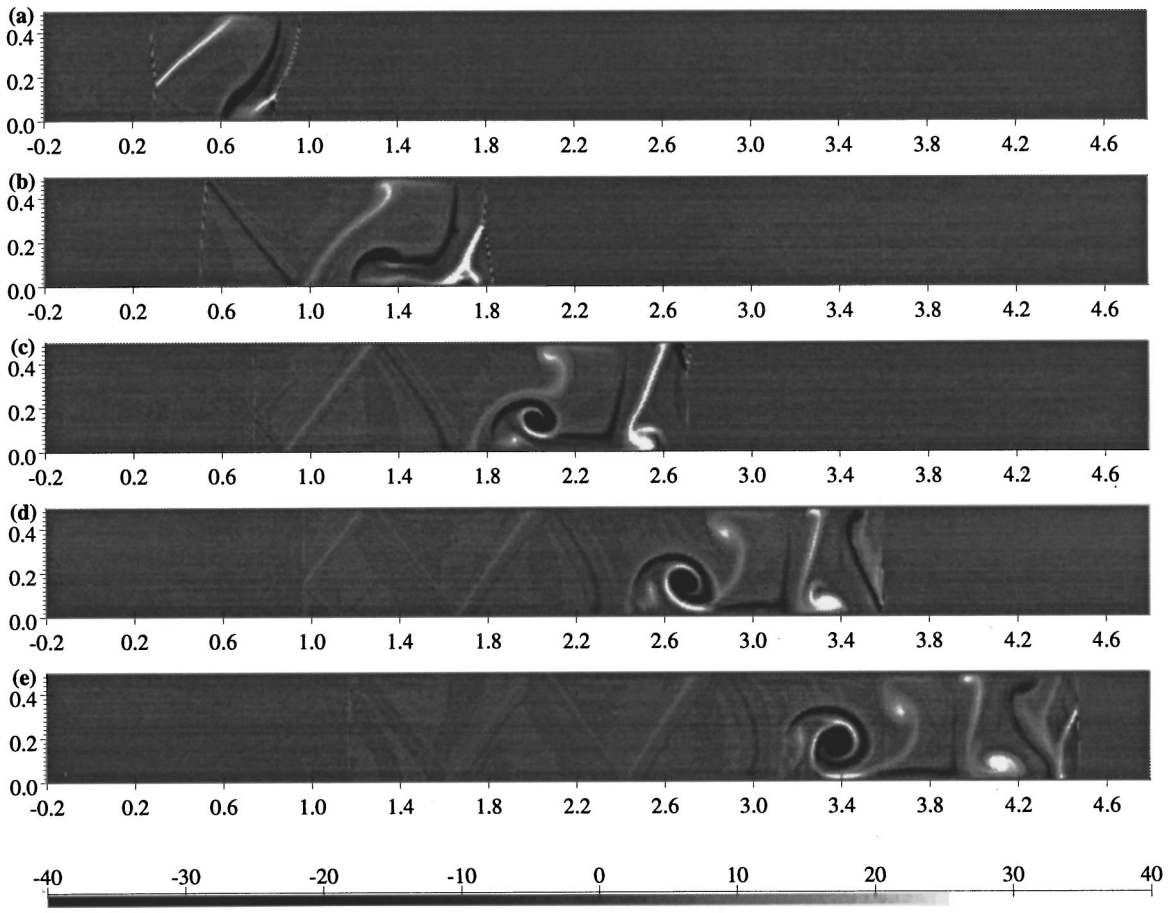

FIG. 22. Time sequence of vorticity images for an $M=10$ shock interaction with a $A_0/\lambda=0.1$ H_2-N_2 interface. Frozen chemistry. Times shown are: (a) 0.166, (b) 0.345, (c) 0.523 (d) 0.700 and (e) 0.878.

etry of the interface appears the same in both cases. The amplitude of the perturbation (plotted in Fig. 18) shows a very small reduction due to dissociation. The growth rate of the amplitude is plotted in Fig. 19. At any instant the frozen and equilibrium limits exhibit different growth rates. The growth rate given by the impulse model (see Fig. 19) overpredicts the growth rate significantly.

We now pose the following question: *Is there a period of linear growth?* The growth rate dA/dt is plotted in Figs. 20 and 21 for frozen and equilibrium cases for a $M=10$ shock interaction with a $A_0/\lambda=0.01$ H_2-N_2 interface. We observe agreement with the linear theory for small times. However nonlinearity manifests itself very rapidly even for this very weakly perturbed interface. Note that the crests and the troughs for the linear and the nonlinear growth rates occur at the same times. It is certainly possible that there exists a sustained period of linear growth of the amplitude but this may require that the initial perturbations (A_0/λ) be extremely small. Nonlinear simulations of smaller perturbations are expensive as very high resolution is required.

In Figs. 22 and 23 vorticity images are shown at various times during the simulation. As the shock traverses the interface, vorticity is generated due to baroclinicity. The interaction between the incident shock and the interface leads to negative baroclinic vorticity on the interface. At the end of this initial rapid interaction, notice the Mach stems associated with the reflected (transmitted) shock near the top (bottom) boundary. The intersections of the Mach stems with the reflected and the transmitted shocks are the location of triple points. Associated with these triple points are shear layers with vorticity opposite in sign to that on the interface. These triple points traverse the reflected (or transmitted) shock fronts and further reflections from the top and bottom boundaries cause the appearance of shear layers (with alternating signs of vorticity). These patterns are very clear in hydrogen. These effects change the circulation budget in the domain. It is precisely these ill-resolved vortex layers that are responsible for the lack of convergence of circulation (see Fig. 14).

The circulation on the interface (interfacial circulation), Γ_i is an important parameter governing the mixing. Γ_i is defined here as the total vorticity for those computational cells containing a mixture of hydrogen and nitrogen. The total circulation in the domain Γ and the interfacial circulation Γ_i is plotted as a function of time in Fig. 24. The shear layers in either hydrogen or nitrogen far from the interface, are relatively unimportant in the mixing process. It is observed that chemical reactions reduce the interfacial circulation only slightly. The horizontal lines in Fig. 24 are theoretical predictions of the primary baroclinic circulation Γ_I at the end of the shock refraction process (see Sec. III C). In this case, fortuitously, the total interfacial circulation is close to the theoretical predictions during the entire simulation. In

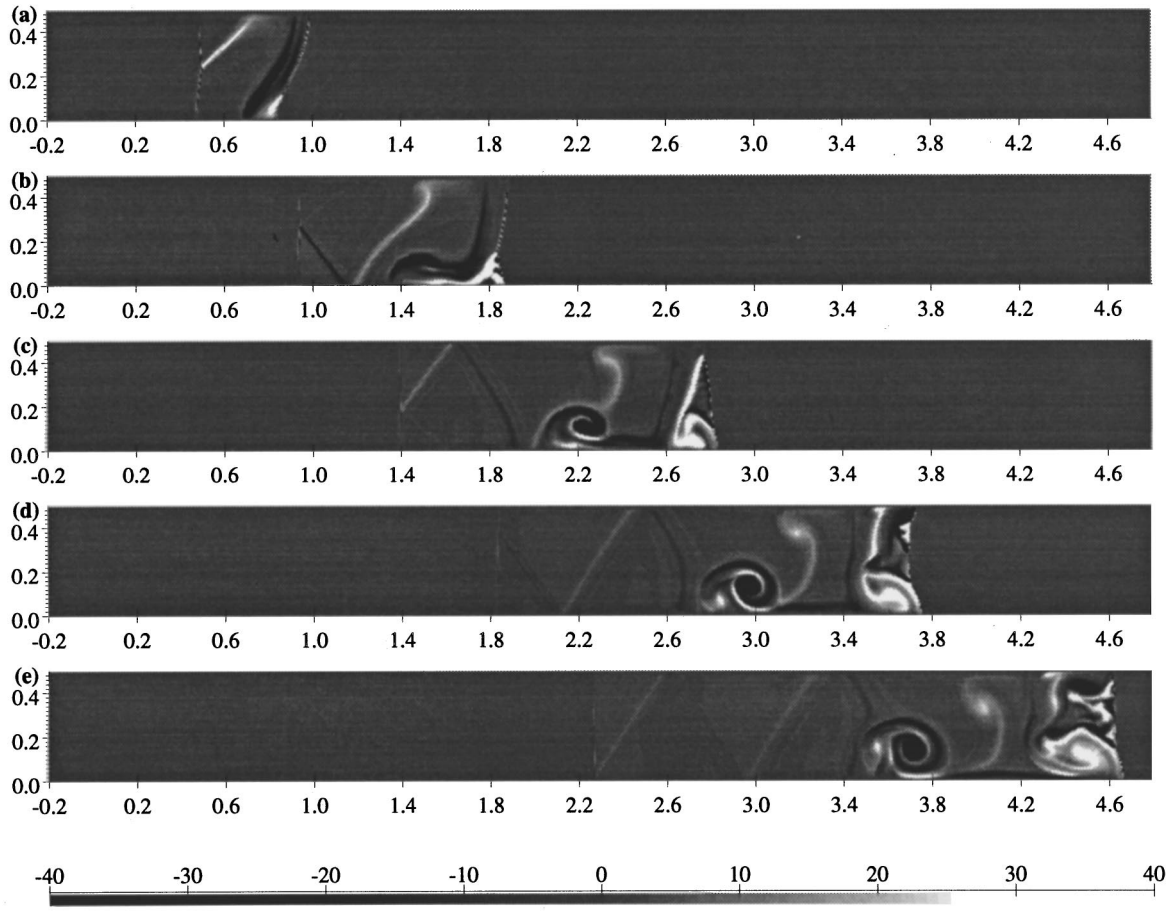

FIG. 23. Time sequence of vorticity images for an $M=10$ shock interaction with a $A_0/\lambda=0.1$ H_2–N_2 interface. Equilibrium chemistry. Times shown are: (a) 0.167, (b) 0.346, (c) 0.524 (d) 0.703 and (e) 0.881.

addition to the total circulation, we quantified the total positive circulation (Γ_p) and total negative circulation (Γ_n). At the end of the simulation, $\Gamma_p=2.66$ and $\Gamma_n=-2.93$, i.e., both these quantities are of comparable magnitude.

Effect of non-equilibrium chemistry: So far we have considered the frozen and the equilibrium limits. In actual practice, the chemical reactions proceed at a finite rate. We consider the interaction of an $M=10$ shock with a H_2–N_2 interface at two different Damköhler numbers, $\Omega=2.06,20.6$. Note that Ω, defined by Eq. (11), is only a reference value. The reaction rate at the shock front is fixed since we have fixed the thermodynamic state of the unshocked hydrogen. Hence different Damköhler numbers are achieved by changing the wavelength of the perturbation.

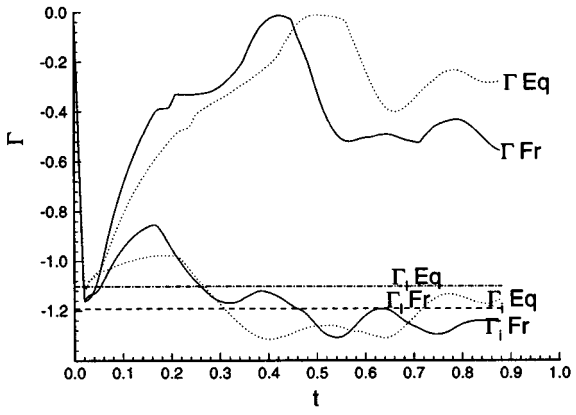

FIG. 24. Total circulation for an $M=10$ shock interaction with a $A_0/\lambda=0.1$ H_2–N_2 interface. The interfacial circulation is denoted by Γ_i. The total circulation is denoted by Γ. The initial baroclinic circulation from local analysis is denoted by Γ_1.

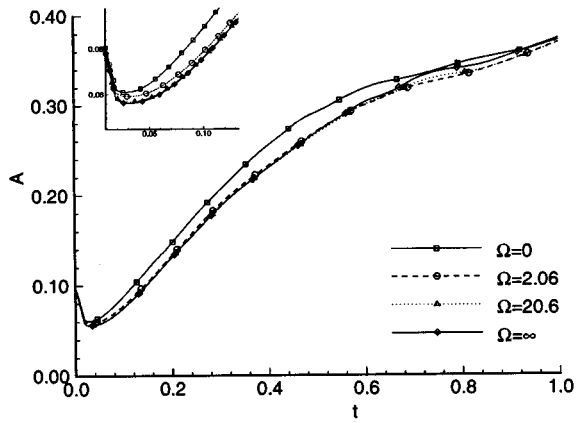

FIG. 25. Amplitude of perturbation A for $M=10$, $A_0/\lambda=0.1$, H_2–N_2 interface for various Damköhler numbers.

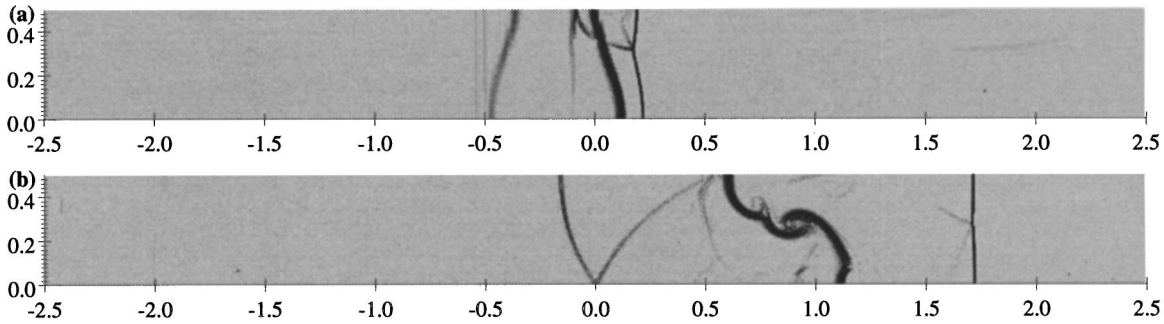

FIG. 26. Time sequence of numerical shadow graphs for an $M=18$ shock interaction with a $A_0/\lambda=0.1$ N_2-H_2 interface. Frozen chemistry. Times shown are: (a) 0.035 and (b) 0.187.

For $\Omega=2.06,20.6$ λ is chosen as 1.0 cm and 0.1 cm, respectively. The amplitude A (normalized by λ) is plotted in Fig. 25. A magnification of the graph corresponding to early times clearly shows that A for finite Ω lies between the frozen and equilibrium limits, albeit closer to the equilibrium chemistry case. This implies that extremely small shock tubes (less than 1 mm width) would be needed to achieve the frozen chemistry limit. Thus, for practical situations, the equilibrium chemistry limit is the relevant one. A smaller Damköhler number than those discussed above, implies a larger relaxation zone behind the incident shock. Resolution of this requires a significantly larger computational domain than is currently feasible. Overall, for the current situation, it appears that finite rate chemistry calculations do not provide any surprises. Therefore, we will not consider finite rate chemical reactions further and focus exclusively on the frozen and equilibrium limits. At late times we see that $A(t)$ for the finite rate chemistry cases lies below the frozen and equilibrium limits which may be due to lack of convergence at late times.

B. High-low acoustic impedance case: N_2-H_2 interface

We next examine the case in which the shock moves from a medium with a low sound speed to a medium with a higher sound speed, characterized by a reflected rarefaction wave. We choose the shock Mach number to be $M=18$ because the effects of chemistry at lower Mach numbers are small. The N_2-H_2 interface is initially perturbed by a single harmonic with $A_0/\lambda=0.1$. The physical domain extent in the x-direction is $[x_l,x_r]\equiv[-2.5\lambda,2.5\lambda]$. In this case, we move the grid with a velocity of 18.26 in the x-direction, which is the average speed of the reflected and transmitted waves. In Figs. 26 and 27 numerical shadowgraph images for the frozen and equilibrium cases are shown at early and late times during the interaction. Unlike the previous case, there is no strong development of the spike in this case. During the refraction process, the transmitted shock moves relatively ahead of the incident shock due to the lower acoustic impedance. Recombination of nitrogen atoms occurs across the rarefaction wave. The peak density in this case occurs behind the incident shock and is $6.9\rho_0$ for the frozen chemistry case and $11.4\rho_0$ for the equilibrium chemistry case. The peak dissociated mass fraction in nitrogen (hydrogen) was 26.7% (4%). For equilibrium chemistry, the temperature behind the incident shock in N_2 is 8175 K thus violating the IDG model. However recombination of N_2 across the rarefaction lowers the peak temperature in N_2 to about 6925 K and thus near the interface the IDG model holds.

In Fig. 28 the amplitude of the interface, $A(t)$, is plotted as a function of time. Even before the shock completely traverses the interface, the interface exhibits a phase reversal i.e., $A(t)$ changes sign and continues to grow in the opposite direction of the initial perturbation. In this case too, we observe a reduction in the growth of the perturbation due to dissociation chemistry.

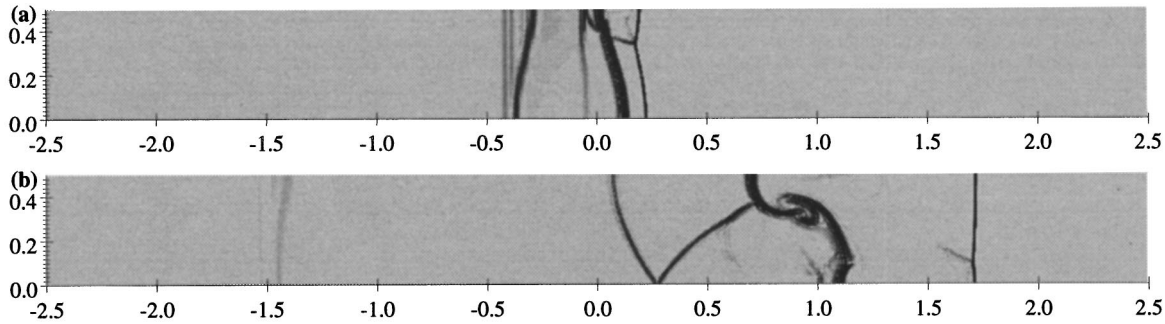

FIG. 27. Time sequence of numerical shadowgraphs for an $M=18$ shock interaction with a $A_0/\lambda=0.1$ N_2-H_2 interface. Equilibrium chemistry. Times shown are: (a) 0.035 and (b) 0.185.

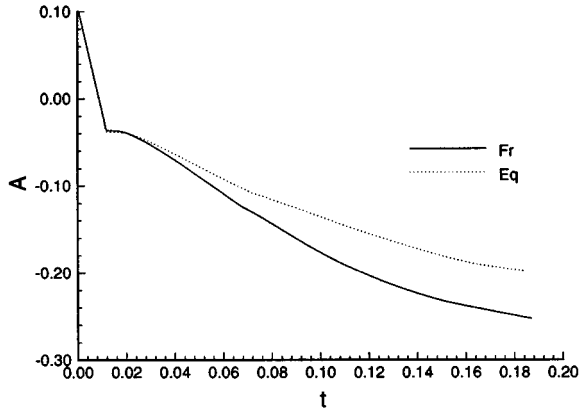

FIG. 28. Amplitude of the perturbation for an $M=18$ shock interaction with a $A_0/\lambda=0.1$ N_2-H_2 interface.

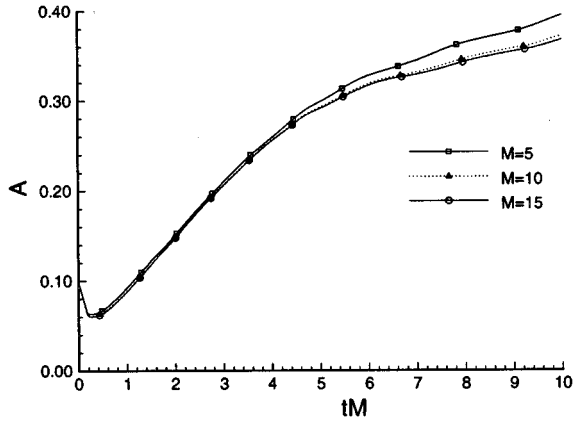

FIG. 30. Amplitude of the perturbation as a function of scaled time (tM) for $M=5,10,15$ shocks. The interface is a $A_0/\lambda=0.1$, H_2-N_2 interface. Frozen chemistry.

In Fig. 29 we plot the total circulation Γ and the inter facial circulation Γ_i as a function of time. After the first peak which is due to the primary baroclinic circulation generation on the interface, there is a sharp reduction in the total circulation. The reason is as follows: the perturbed transmitted shock becomes planar (under normal circumstances shocks are stable) and this is achieved via compression waves, which steepen and form a shock and a Mach stem in hydrogen. In fact these waves interact with the interface and generate vorticity of opposite sign. The angle between the interface and the waves is quite large. In addition, the time of interaction is larger relative to the incident shock passage time. Thus, this secondary interaction leads to a larger baroclinic generation of vorticity of opposite sign than the primary interaction of the incident shock with the interface. As observed for the H_2-N_2 interface case, there is a reverberation of these waves from the lines of symmetry and this is responsible for the oscillations seen in the plot of circulation. Note that Γ_i shows a smaller variation with time than Γ. The horizontal dotted lines in Fig. 29 are the theoretical prediction of the primary baroclinic circulation generation Γ_1 by the incident shock.

C. Mach number scaling

Note that the hydrodynamic equations for the frozen and equilibrium chemistry cases are invariant under the following transformation:

$$t\rightarrow tM, p\rightarrow p/M^2, u\rightarrow u/M, E\rightarrow E/M^2. \tag{46}$$

It is also well-known that for high Mach number perfect gas flows that the pressure and the velocity behind a shock scale quadratically and linearly in Mach number M. We expect that the above scaling holds for the frozen cases discussed above and furthermore we are interested in departure from the above scaling in the presence of chemistry.

In Figs. 30 and 31, the amplitude is plotted as a function of tM, i.e., time scaled by the Mach number of the shock for both the frozen and the equilibrium case for the H_2-N_2 interface. Furthermore, we examine the scaled growth rate $(dA/dt)/M$ and the scaled circulation Γ/M in Figs. 32, 33, 34 and 35, respectively. For the frozen limit, the above Mach number scaling holds for the entire duration of the simulation. We believe that such a detailed agreement of the scaled results for frozen high M flows has not been reported previ-

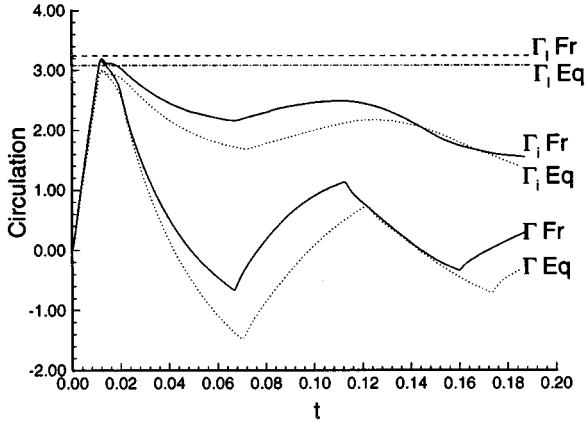

FIG. 29. Circulation for an $M=18$ shock interaction with a $A_0/\lambda=0.1$ N_2-H_2 interface. The interfacial circulation is denoted by Γ_i. The total circulation is denoted by Γ. The initial baroclinic circulation from local analysis is denoted by Γ_1.

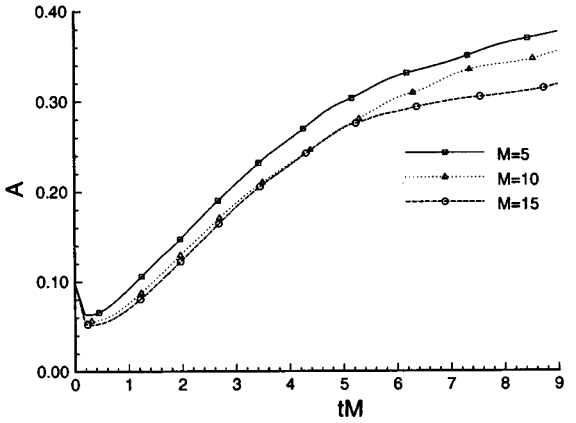

FIG. 31. Amplitude of the perturbation as a function of scaled time (tM) for $M=5,10,15$ shocks. The interface is a $A_0/\lambda=0.1$, H_2-N_2 interface. Equilibrium chemistry.

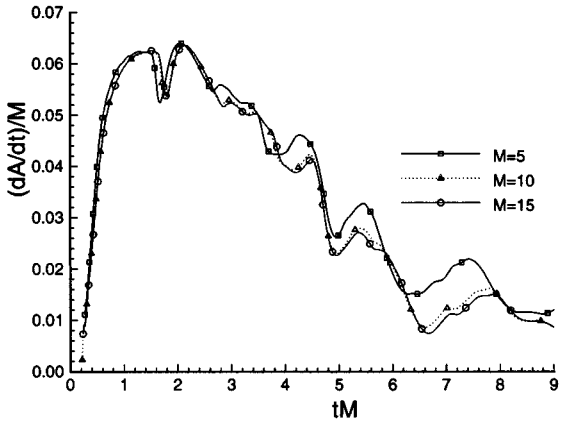

FIG. 32. Scaled growth rate $(dA/dt/M)$ as a function of scaled time (tM) for $M=5,10,15$ shocks. The interface is a $A_0/\lambda=0.1$, H_2-N_2 interface. Frozen chemistry.

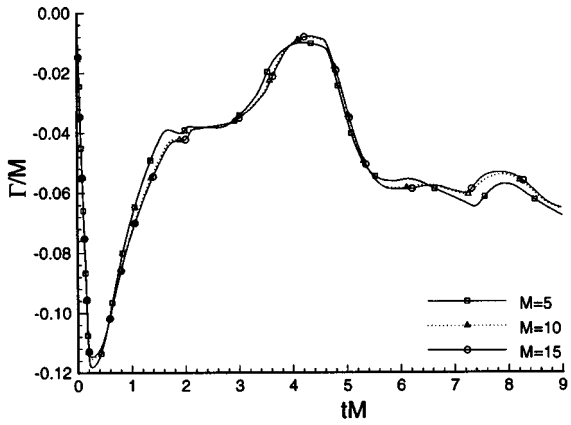

FIG. 34. Scaled circulation (Γ/M) as a function of scaled time (tM) for $M=5,10,15$ shocks. The interface is a $A_0/\lambda=0.1$, H_2-N_2 interface. Frozen chemistry.

ously. The scaling for the equilibrium limit is not as good as for the frozen limit. However for the amplitude, the differences between the scaled curves are small and we observe a monotonic decrease in $A(t)$ with increase in M in the presence of equilibrium chemistry.

For the N_2-H_2 interface, the scaled circulation, Γ/M and amplitude A are plotted as a function of scaled time, tM for frozen and equilibrium cases in Figs. 36, 37, 38 and 39. For this case too, Mach number scaling holds for the frozen limit.

VII. SIMULATION RESULTS: LOW ATWOOD RATIO INTERFACES

Until now, we have examined the high density ratio cases (pre-shock Atwood number, $At=\pm 0.867$). For the high Atwood number cases, we observe that the effects of dissociation, in as much as the perturbation growth is concerned, are quite small except for very high Mach numbers. In this section, we briefly examine the low Atwood number cases i.e., N_2-O_2 or O_2-N_2 interfaces (preshock Atwood number, $At=\pm 0.067$).

A. Low-high acoustic impedance case: N_2-O_2 interface

We examine the case of a $M=12$ shock incident in nitrogen. During refraction, the reflected shock is a very weak shock. In this case, equilibrium chemistry plays an important role in oxygen which has a much lower dissociation temperature than nitrogen. We remind the reader that no reaction between the two gases at the interface is allowed, i.e., NO formation is completely suppressed. The linear theory indicates a higher growth rate in the presence of equilibrium chemistry (see Sec. IV). The nonlinear simulations also indicate that the growth rate of the perturbation amplitude $A(t)$ (Fig. 40) is larger in the presence of equilibrium chemistry. However note that the growth of the perturbations is extremely slow. The initial compression of the perturbation amplitude is large and for the times shown the perturbation amplitude has not even recovered its original unshocked value. We did not carry out the simulations further in time because we have already exceeded what would be a reasonable duration in an experiment in T5. In this case, the im-

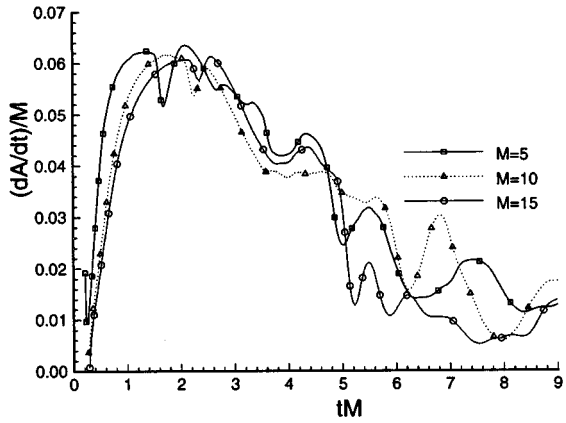

FIG. 33. Scaled growth rate $(dA/dt/M)$ as a function of scaled time (tM) for $M=5,10,15$ shocks. The interface is a $A_0/\lambda=0.1$, H_2-N_2 interface. Equilibrium chemistry.

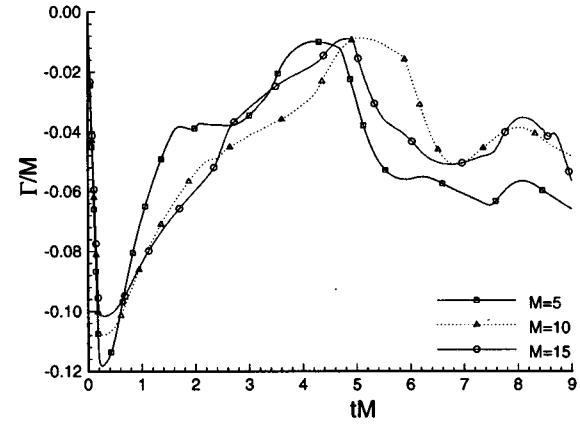

FIG. 35. Scaled circulation (Γ/M) as a function of scaled time (tM) for $M=5,10,15$ shocks. The interface is a $A_0/\lambda=0.1$, H_2-N_2 interface. Equilibrium chemistry.

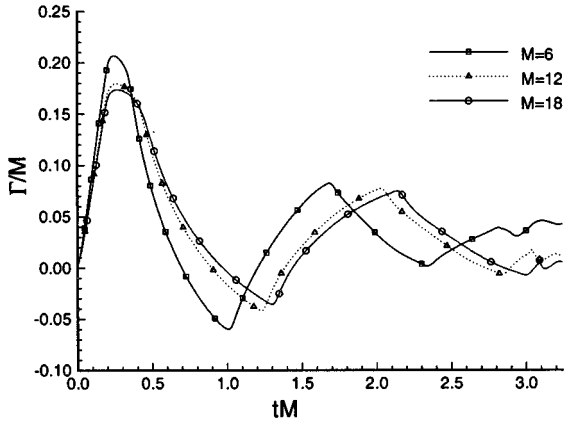

FIG. 36. Scaled circulation versus scaled time for a $A_0/\lambda = 0.1$ N_2-H_2 interface. Frozen chemistry.

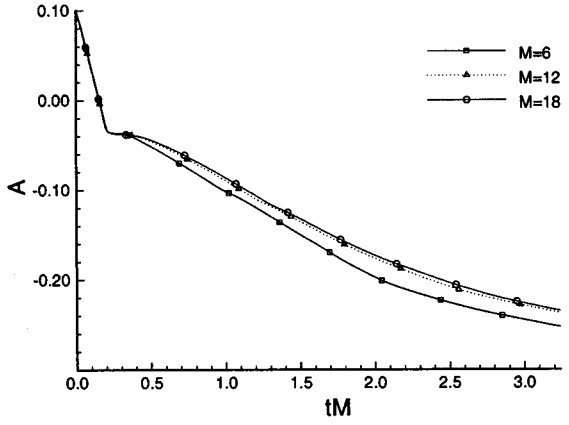

FIG. 38. Amplitude of the perturbation versus scaled time for a $A_0/\lambda = 0.1$ N_2-H_2 interface. Frozen chemistry.

pulse model is inaccurate and should not be employed for predicting growth rates for either the frozen or the equilibrium chemistry case. We will not dwell upon this rather uninteresting case any further except to state that the primary baroclinic circulation generation is larger for the equilibrium chemistry case than the frozen chemistry case (see Table II).

B. High-low acoustic impedance case: O_2-N_2 interface

In this case, the circulation on the interface is larger for the equilibrium case than the frozen case at early times. The perturbation amplitude $A(t)$ is larger for the equilibrium case and is overtaken by the frozen case only at late times. The dissociation behind the incident shock ($M=12$) in oxygen is about 21%. The overall conclusion is that chemistry seems to play a significant role at lower Atwood numbers in changing the primary baroclinic circulation generation. However, the growth of the perturbations is observed to be extremely slow and we conjecture that experiments of these low Atwood number cases one would not observe any significant mixing.

VIII. CONCLUSION

In this paper, we have examined the effects of dissociation in the interaction of shocks with density interfaces under hypervelocity conditions. For the high Atwood number interfaces examined, dissociation chemistry increases the peak density and reduces the peak temperature significantly. A small reduction in the growth of the perturbations is also observed due to dissociation chemistry. We developed a local analysis which may be used to get a self-similar solution for weakly perturbed (small β_0) sawtooth interfaces. Furthermore, the local analysis shows that the change due to dissociation in the primary baroclinic circulation generation is small for high Atwood number interfaces. For strong shocks and in the absence of chemistry it is appropriate to scale the time by M, and the growth rate and the circulation by $1/M$. For the initial thermodynamic conditions examined, the equilibrium chemistry limit appears appropriate. The frozen limits will be achieved for extremely small, and hence impractical length scales. For low Atwood number interfaces, we observed that the primary baroclinic circulation generation and the growth rate was larger in the presence of

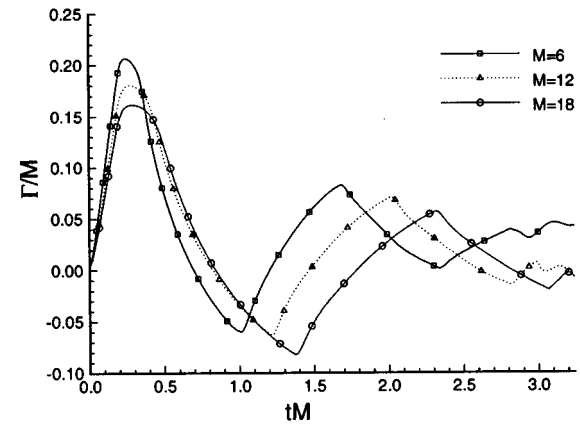

FIG. 37. Scaled circulation versus scaled time for a $A_0/\lambda = 0.1$ N_2-H_2 interface. Equilibrium chemistry.

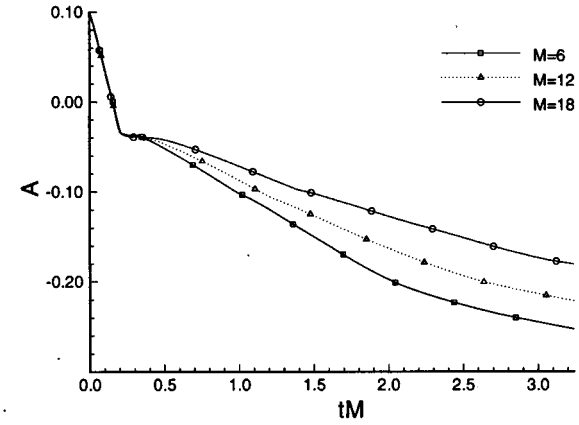

FIG. 39. Amplitude of the perturbation versus scaled time for a $A_0/\lambda = 0.1$ N_2-H_2 interface. Equilibrium chemistry.

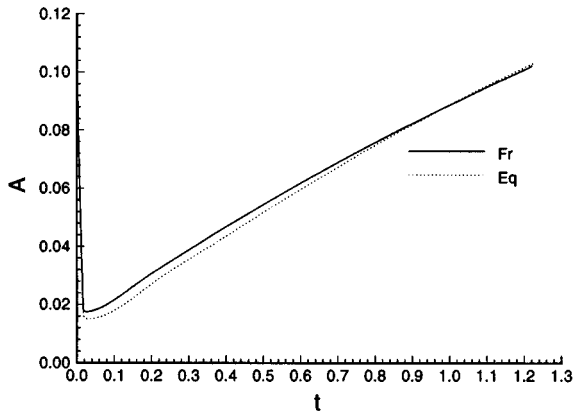

FIG. 40. Amplitude of the perturbation for an $M=12$ shock interaction with a $A_0/\lambda=0.1$ N_2-O_2 interface.

equilibrium chemistry. The growth of the perturbation for very strong shocks and low Atwood numbers was extremely small.

For the case of a reflected shock wave, we extended Richtmyer's linear theory and impulse model to include equilibrium chemistry. Good agreement between the linear theory and nonlinear simulations was observed for $A_0/\lambda=0.01$ at early times while departure from the linear theory occurred rapidly even for these weakly perturbed interfaces. We conclude that for the strong incident shocks there is no sustained period of linear growth.

In the future, we hope to go beyond the simple IDG model and implement changes in vibrational energy. Furthermore, we hope to implement a more realistic chemistry model with a larger gamut of chemical reactions.

ACKNOWLEDGMENTS

This work was supported in part by AFOSR Grant No. F49620-93-1-0338 and by the Lawrence Livermore National Laboratory under subcontract B295121 under DOE Contract W-7405-ENG-48. This research was performed in part using the CSCC parallel computer system operated by Caltech on behalf of the Concurrent Supercomputing Consortium. We acknowledge discussions with Professor Dale Pullin and useful comments by Mark Meloon. RS acknowledges the help of Berna Massingill who provided the mesh archetypes for the Intel Paragon and Thanh Phung who helped optimize the code.

APPENDIX: NUMERICAL METHOD DETAILS

We first present details of the hydrodynamical part of the solution of the equations, i.e., Eq. (2) with no source term. Let $\mathbf{U}_{ij}^n$ be the approximation to the solution $\mathbf{U}(x_i,y_j,t_n)$ of Eq. (2) in the (i,j)th cell where $x_i=x_l+i\Delta x$, $y_j=j\Delta y$ and $t_n=n\Delta t$. The time integration procedure is:

$$\mathbf{U}_{ij}^{n+1/2}=\mathbf{U}_{ij}^n-\frac{\Delta t}{2}\left(\frac{\mathbf{F}_{i+1/2,j}^n-\mathbf{F}_{i-1/2,j}^n}{\Delta x}+\frac{\mathbf{G}_{i,j+1/2}^n-\mathbf{G}_{i,j-1/2}^n}{\Delta y}\right), \tag{A1}$$

$$\mathbf{U}_{ij}^{n+1}=\mathbf{U}_{ij}^n-\Delta t\left(\frac{\mathbf{F}_{i+1/2,j}^{n+1/2}-\mathbf{F}_{i-1/2,j}^{n+1/2}}{\Delta x}+\frac{\mathbf{G}_{i,j+1/2}^{n+1/2}-\mathbf{G}_{i,j-1/2}^{n+1/2}}{\Delta y}\right). \tag{A2}$$

The flux of mass, momentum, energy and the mass fractions through the cell interface at $x_{i+1/2}\equiv x_i+\Delta x/2$ is

$$\mathbf{F}_{i+1/2,j}\equiv\mathbf{F}(\mathbf{V}_l,\mathbf{V}_r)_{i+1/2,j}, \tag{A3}$$

where $\mathbf{V}_l$ and $\mathbf{V}_r$ are the left and right states at the cell interface $x_{i+1/2}$ obtained by a linear reconstruction from the value of $\mathbf{V}$ in (i)th, $(i-1)$th and the $(i+1)$th cells. $\mathbf{V}$ is simply the vector of unconserved variables given by

$$\mathbf{V}=\{\rho,u,v,p,\rho_1/\rho,\alpha_1,\alpha_2\}^T. \tag{A4}$$

According to EFM, the flux vector is given by (dropping the $i+1/2,j$ subscript)

$$\mathbf{F}(\mathbf{V}_l,\mathbf{V}_r)=\mathbf{F}(\mathbf{V}_l)+\mathbf{F}(\mathbf{V}_r), \tag{A5}$$

$$\mathbf{F}(\mathbf{V})=\begin{bmatrix} F_{\text{mass}} \\ \left(u^2+\frac{c_p^2}{2}\right)\rho W+\rho u c_p D \\ vF_{\text{mass}} \\ \left(\frac{u^2+v^2}{2}+\frac{\gamma}{\gamma-1}\frac{c_p^2}{2}\right)\rho uW+\left(\frac{u^2+v^2}{2}+\frac{\gamma+1}{\gamma-1}\frac{c_p^2}{4}\right)\rho c_p D+\sum_k\frac{\rho_k\alpha_k}{\rho}\theta_{d,k}R_kF_{\text{mass}} \\ \frac{\rho_1}{\rho}F_{\text{mass}} \\ \frac{\rho_1\alpha_1}{\rho}F_{\text{mass}} \\ \frac{\rho_1\alpha_2}{\rho}F_{\text{mass}} \end{bmatrix}. \tag{A6}$$

In the above equation $F_{mass}=\rho u W+\rho c_p D$, $c_p=(2RT)^{1/2}$ is the most probable sound speed and

$$W=\begin{cases} \dfrac{1+erf(u/c_p)}{2} & \text{if } \mathbf{V}=\mathbf{V}_l \\ \dfrac{1-erf(u/c_p)}{2} & \text{if } \mathbf{V}=\mathbf{V}_r, \end{cases}$$

$$D=\begin{cases} \dfrac{1}{2\sqrt{\pi}}\exp(u^2/c_p^2) & \text{if } \mathbf{V}=\mathbf{V}_l \\ -\dfrac{1}{2\sqrt{\pi}}\exp(u^2/c_p^2) & \text{if } \mathbf{V}=\mathbf{V}_r. \end{cases}$$

The linear reconstruction procedure is as follows. The left and right states at the interface $x_{i+1/2}$ are given by

$$\mathbf{V}_l=\mathbf{V}_i+\frac{\Delta x}{2}\left(\frac{\partial \mathbf{V}}{\partial x}\right)_i,$$
$$\mathbf{V}_r=\mathbf{V}_{i+1}-\frac{\Delta x}{2}\left(\frac{\partial \mathbf{V}}{\partial x}\right)_{i+1}. \tag{A7}$$

The slope in cell i is given by

$$\left(\frac{\partial \mathbf{V}}{\partial x}\right)_i=[L]_i^{-1}\text{minmod}(\tilde{\mathbf{V}}_i,\tilde{\mathbf{V}}_{i+1},\tilde{\mathbf{V}}_{i-1}), \tag{A8}$$

where $\tilde{\mathbf{V}}_{i+k}=[L]_i\mathbf{V}_{i+k}$, $k=-1,0,1$ is the projection of $\mathbf{V}$ on to the characteristic space, and the *minmod* function provides the slope limiting.[26] The matrix of left eigenvectors of the Jacobian $\partial\mathbf{F}/\partial\mathbf{V}$, is $[L]_i$ given by

$$[L]=\begin{bmatrix} 0 & \rho/2 & 0 & -1/(2c) & 0 & 0 & 0 \\ c & 0 & 0 & -1/c & 0 & 0 & 0 \\ 0 & 0 & 1 & 0 & 0 & 0 & 0 \\ 0 & \rho/2 & 0 & 1/(2c) & 0 & 0 & 0 \\ 0 & 0 & 0 & 0 & 1 & 0 & 0 \\ 0 & 0 & 0 & 0 & 0 & 1 & 0 \\ 0 & 0 & 0 & 0 & 0 & 0 & 1 \end{bmatrix}. \tag{A9}$$

We now present details of the chemistry stage in the solution of the governing equations. This stage is necessary only for $\Omega\neq 0$ and is carried out after the hydrodynamical step. During the chemistry stage, we update the mass fractions α_1 and α_2, and the temperature T in each computational cell. The total energy E in each computational cell is constrained to be constant. Since during this step, there is no flow across the cell boundaries, we actually keep the total specific internal energy e constant. This implies the following relation between T, α_1 and α_2

$$T=T_0+\sum_k T_k\alpha_k, \tag{A10}$$

$$T_0=\frac{\rho e}{3(\rho_1 R_1+\rho_2 R_2)},$$
$$T_k=\frac{-\rho_k\theta_{d,k}R_k}{3(\rho_1 R_1+\rho_2 R_2)}. \tag{A11}$$

For $\Omega\to\infty$, the following two equations (the law of mass action rewritten for each gas under the constraint that the total energy remains constant) are solved by a Newton–Raphson technique:

$$f_1(\alpha_1,\alpha_2)\equiv\rho_1\alpha_1^2-(1-\alpha_1)\rho_{d,1}\exp\left(\frac{-\theta_{d,1}}{T_0+\Sigma_k T_k\alpha_k}\right)=0, \tag{A12}$$

$$f_2(\alpha_1,\alpha_2)\equiv\rho_2\alpha_2^2-(1-\alpha_2)\rho_{d,2}\exp\left(\frac{-\theta_{d,2}}{T_0+\Sigma_k T_k\alpha_k}\right)=0. \tag{A13}$$

For finite Ω Eq. (5) is integrated in time from t_n to $t_n+\Delta t_c$ where Δt_c equals either $\Delta t/2$ or Δt depending upon whether this is done after the first or the second time integration stage of the hydrodynamical equations. Let $\alpha_k^{n+1/2}\equiv\alpha_k(t_n+\Delta t_c/2)$ and $\alpha_k^{n+1}\equiv\alpha_k(t_n+\Delta t_c)$. Then, the first stage of the implicit integration method is given below:

$$\alpha_k^{n+1/2}=\alpha_k^n+\frac{\Delta t_c}{2}\left(\frac{d\alpha_k}{dt}\right)^{n+1/2}, \tag{A14}$$

where the reaction rate is expressed as

$$\left(\frac{d\alpha_k}{dt}\right)^{n+1/2}=C_k(T^{n+1/2})\rho_k\left[(1-\alpha_k^{n+1/2})\times\exp\left(\frac{-\theta_{d,k}}{T^{n+1/2}}\right)-\frac{\rho_k}{\rho_{d,k}}(\alpha_k^2)^{n+1/2}\right]. \tag{A15}$$

The second stage of the implicit integration is given as

$$\alpha_k^{n+1}=\alpha_k^n+\frac{\Delta t_c}{2}\left[\left(\frac{d\alpha_k}{dt}\right)^{n+1/2}+\left(\frac{d\alpha_k}{dt}\right)^{n+1}\right], \tag{A16}$$

where

$$\left(\frac{d\alpha_k}{dt}\right)^{n+1}=C_k(T^{n+1})\rho_k\left[(1-\alpha_k^{n+1})\times\exp\left(\frac{-\theta_{d,k}}{T^{n+1}}\right)-\frac{\rho_k}{\rho_{d,k}}(\alpha_k^2)^{n+1}\right]. \tag{A17}$$

In both the stages we must take care that the temperature is expressed appropriately i.e. $T^{n+l}=T_0+\Sigma_k T_k\alpha_k^{n+l}$, $l=1/2,1$. During each implicit integration stage the solution was obtained by Newton–Raphson.

[1] In *Proceedings of the 4th International Workshop on the Physics of Compressible Turbulent Mixing*, 1993, edited by P. F. Linden, D. L. Youngs, and S. B. Dalziel (Cambridge University Press, Cambridge, England, 1993).

[2] R. D. Richtmyer, ''Taylor instability in shock acceleration of compressible fluids,'' Commun. Pure Appl. Math. **XIII**, 297 (1960).

[3] E. E. Meshkov, ''Instability of the interface of two gases accelerated by a shock wave,'' Fluid Dynam. **4**, 101 (1969) [translated from Izv. Akad. Nauk. SSSR, Mekh. Zhidk. Gaza **5**, 151 (1969)].

[4] J. W. Grove, R. Holmes, D. H. Sharp, Y. Yang, and Q. Zhang, ''Quantitative theory of Richmyer-Meshkov instability,'' Phys. Rev. Lett. **71**, 3473 (1993).

[5] R. L. Holmes, J. W. Grove, and D. Sharp ''Numerical investigation of

Richtmyer-Meshkov instability using front tracking,'' J. Fluid Mech. **301**, 51 (1995).
[6]J. D. Lindl, R. L. McCrory, and E. M. Campbell ''Progress toward ignition and burn propagation in inertial confinement fusion,'' Phys. Today **45** (9), 32 (1992).
[7]W. D. Arnett, J. N. Bahcall, R. P. Kirshner, and S. E. Woosley, ''Supernova 1987A,'' Annu. Rev. Astron. Astrophys. **27**, 629 (1989).
[8]P. Miller, T. A. Peyser, P. E. Stry, and K. S. Budil, ''Shock-hydrodynamics experiments on the Nova laser,'' in *Proceedings of the 20th International Symposium on Shock Waves*, edited by B. Sturtevant, J. E. Shepherd, and H. G. Hornung (World Scientific, Singapore, 1996).
[9]B. Sturtevant (private communication, 1995).
[10]W. G. Vincenti and C. H. Kruger, *Physical Gas Dynamics* (Wiley, New York, 1965).
[11]R. Samtaney and D. I. Pullin, ''On initial-value and self-similar solutions of the compressible Euler equations,'' Phys. Fluids **8**, 2650 (1996).
[12]M. J. Lighthill, ''Dynamics of a dissociating gas. Part 1. Equilibrium flow,'' J. Fluid Mech. **2**, 1 (1957).
[13]N. C. Freeman, ''Non-equilibrium flow of an ideal dissociating gas,'' J. Fluid Mech. **4**, 407 (1958).
[14]Y. Yang, Q. Zhang, and D. H. Sharp, ''Small amplitude theory of Richtmyer–Meshkov instability,'' Phys. Fluids **6**, 1856 (1994).
[15]A. M. Abd-El-Fattah and L. F. Henderson, ''Shock waves at a fast-slow gas interface,'' J. Fluid Mech. **86**, 15 (1978).
[16]L. F. Henderson, P. Colella, and E. G. Puckett, ''On the refraction of shock waves at a slow-fast gas interface,'' J. Fluid Mech. **224**, 1 (1991).
[17]R. Samtaney and N. J. Zabusky, ''Circulation deposition on shock-accelerated planar and curved density-stratified interfaces: models and scaling laws,'' J. Fluid Mech. **269**, 45 (1994).
[18]R. Samtaney, J. Ray, and N. J. Zabusky, ''Scaling laws for vorticity generation on shock-accelerated slow-fast interfaces'' (in preparation).
[19]D. I. Pullin, ''Direct simulation methods for compressible ideal gas flow,'' J. Comput. Phys. **34**, 231 (1980).
[20]M. N. Macrossan, ''The equilibrium flux method for the calculation of flows with non-equilibrium chemical reactions,'' J. Comput. Phys. **80**, 204 (1989).
[21]K. M. Chandy, R. Manohar, B. L. Massingill, and D. I. Meiron, ''Integrating task and data parallelism with the group communication archetype,'' in *Proceedings of the 9th International Parallel Processing Symposium*, 1995 (unpublished).
[22]R. F. Benjamin, ''Experimental observations of shock stability and shock-induced turbulence,'' in *Advances in Compressible Turbulent Mixing*, edited by A. Buckingham, C. Leith, and W. Dannevik, DOE Publication Conf. No. 8810234 (1992).
[23]M. Meloon (private communication, 1996).
[24]W. Mulder, S. Osher, and J. A. Sethian, ''Computing interface motion in compressible gas dynamics,'' J. Comput. Phys. **100**, 209 (1992).
[25]R. Courant and K. O. Friedrichs, *Supersonic Flow and Shock Waves* (Springer, Berlin, 1948).
[26]B. Van Leer, ''Towards the ultimate conservative difference scheme IV: A new approach to numerical convection,'' J. Comput. Phys. **23**, 276 (1977).